Master's Thesis

Combination of Reactivity Experiments with
High-Resolution Scanning Probe Microscopy Studies

Hendrik Ronneburg
Course of Studies: Chemistry

1. Examiner:
Prof. Dr. H.-J. Freund
Fritz-Haber-Institut der MPG
Faradayweg 4-6
14195 Berlin

2. Examiner:
Prof. Dr. T. Risse
Institut für Chemie der FU Berlin
Takustraße 3
14195 Berlin

Hand-in date: 19.07.2013

This thesis was performed under the supervision of Dr. M. Heyde in the AFM group at the chemical physics department of the Fritz-Haber-Institut der Max-Planck-Gesellschaft during the time of the 1st October 2012 until the 19th July 2013.

During this thesis a poster was presented and a talk was held at the Deutsche Physikalische Gesellschaft Spring Meeting of the Condensed Matter Section. The presented poster can be found in the attachment.

Technical drafts of the implemented UHV-parts are also attached.

Abbreviations

AES – Auger-electron spectroscopy
c.h. – constant height
CPD – contact potential differences
FER – field emission resonance
FM – Frank-van der Merwe
LEED – low energy electron diffraction
ML – monolayer
MS – mass spectrometry
nc-AFM – non-contact atomic force microscopy
Ref. – reference
SK – Stranski-Krastanov
STM – scanning tunnelling microscopy
STS – scanning tunnelling spectroscopy
TPD – temperature programmed desorption
UHV – ultra-high vacuum
VW – Volmer-Weber

Table of contents

1. Introduction

Huge amounts of chemicals are used to fabricate many industrial products of our modern world. Catalysts are used for lowering activation barriers of chemical reactions. This can lead to an acceleration of these reactions, the increase of energetic efficiency, the suppression of byproducts and higher production efficiency. Therefore catalysts play an important role in modern chemistry.

If educts and catalysts are present in a different state of matter this refers to heterogeneous catalysis, otherwise to homogeneous catalysis. In the former case usually a mobile phase is flowed over a solid phase containing the catalyst. During this flow process the educts adsorb, react on the catalyst surface, desorb and restore the active catalyst state.[1]

Industrial used catalysts have a very complex structure. They are usually formed under reaction conditions, exhibit a complex three-dimensional structures and may therefore not be accessible by surface specific methods. As an approach to industrial used catalysts model catalysts were developed. These model catalysts often consist of oxide layers on a metal single crystal substrate. These model catalysts are due to their atomically flat surface and and their conductivity accessible to surface science methods. It was shown, that MgO films on different metal substrates can be used as model catalysts for heterogeneous catalysis.[2] Thin MgO films are strongly affected by the underlying metal substrates. For example the work function of the model catalyst and the morphology of its MgO film can be tuned by the choice of metal substrate and film thickness.[3,4] A deeper understanding of the mechanisms involved herein is desired to gain insight in the interaction of the educts and products with the catalyst.

Defects and other morphological features have been shown to exhibit electronic properties varying from flat terraces (e. g. charge trapping[5]). A method that is able to distinguish such features from the residual surface is required for studying surfaces in detail, as these features may have an influence on the reactivity. Combined non-contact atomic force and scanning tunnelling microscopy (nc-AFM/STM) is such a method. It can monitor the morphology and electronic structure in real space with atomic resolution.[6]

Additionally a method to study the reactivity of the model catalysts is needed. For the investigation of the interaction of molecules with a surface temperature programmed desorption (TPD) can be used. It can provide information on the binding of molecules to the surface.

The research aims of this project are to combine the TPD reactivity studies with investigations of the morphology and electronic structure via nc-AFM/STM[7], low energy electron diffraction (LEED) and Auger-electron spectroscopy (AES). The chosen model catalysts consist of MgO films deposited on one of three different metal substrates, namely Fe(001), Ag(001) or Mo(001). The MgO films can either be pristine or doped. The scheme of the project is visualized in figure 1.1.

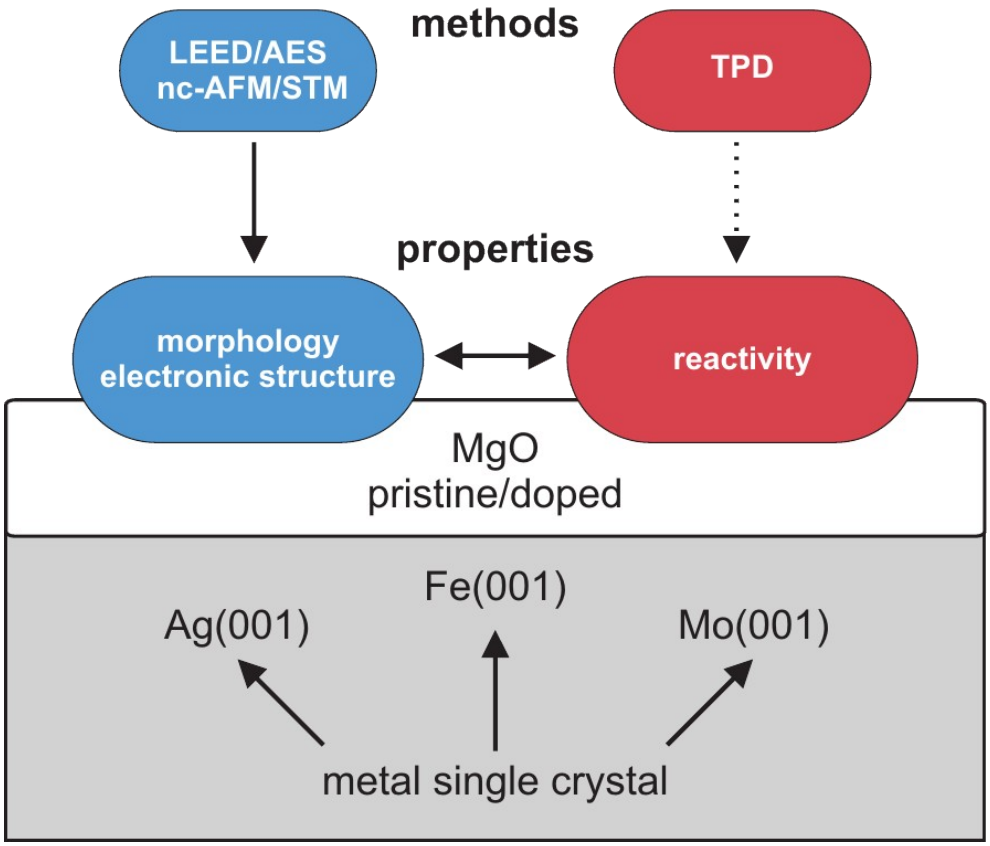

Figure 1.1: Scheme of the research project.

For doping MgO films, one has to avoid segregation of dopants into the substrate, which can be achieved with thicker films (e.g. >30 monolayers). This thickness of MgO films has not resulted in flat films on Ag(001), necessary for nc-AFM/STM investigation.[8] On Mo(001) the annealing is usually done at higher temperatures, which might lead to problems with the portable sample setup (see chapter 2.7). Therefore a method to use thick MgO films in doping experiments compatible with the portable sample setup was required. Two approaches were investigated: On the one hand a

cleaning procedure for Mo(001) that requires lower temperatures and on the other hand using Fe(001) as a substrate for MgO film deposition. Deposition of MgO on Fe(001) has been reported to require lower temperatures than for Mo(001).

Additionally during this thesis preliminary works for the implementation of a TPD setup have been carried out.

In the following pages first a brief explanation of the used methods, general concepts and the design of the used UHV-chamber will be presented. Additionally its parts and the preliminary considerations for the implementation of the temperature programmed desorption are described.
Then the results of the implementation, the cleaning procedures and the investigation of MgO on Fe(001) will be presented and compared to literature.

2. Methods, techniques and design

This chapter will give a short overview on the theory, which is necessary to understand what was achieved during this thesis, and introduce to the general concepts and the design of the used UHV chamber. It will begin with an introduction to UHV and different growth modes of thin films within it. Then low energy electron diffraction and Auger electron spectroscopy will be introduced. Both methods are used for an integrating investigation of the surface, whereas with the former one can obtain information on the surface structure and with the latter on its elemental composition.
Subsequently the main methods of the working group are presented briefly: combined non-contact atomic force and scanning tunnelling microscopy. These methods are able to provide real space images and spectroscopic data for investigating surface morphology and electronic structure.
In the end temperature programmed desorption and its basic ideas are introduced. Also the current chamber design and the changes for the implementation of the TPD setup will be presented.

2.1. Ultra-high vacuum systems and thin films growth

For precisely defined adsorption and desorption conditions the model catalysts are investigated in UHV. This means a negligible influence of gas molecule collisions with the sample surface during experiments. A base pressure of about 10^{-10} hPa is usually used for this. At this low pressure the influence of residual gas molecules can be neglected for usual experimental time scales and vapour deposition methods can be applied to deposit thin films of high chemical purity.
When considering thin films, three growth modes are known[9]: Frank-van der Merwe (FM), Stranski-Krastanov (SK) and Volmer-Weber (VW).
For understanding these growth modes the use of the surface free energy is useful. This energy γ is defined as the change of Gibbs free energy G, upon formation of new surface area A at no change in temperature T or pressure p (equation 2.1).

$$y = \left(\frac{\partial G}{\partial A} \right)_{p,T} \tag{2.1}$$

The FM and SK growth modes are also called layer-by-layer and layer-plus-island growth, respectively. Both can be observed, if the binding energy of the adsorbing particles to each other is lower than to the surface of the bulk.
Upon further film material deposition the sum of the surface free energies of the created and vanishing surfaces as well as the energy of formation of the inner film layers determine the further growth behaviour. This may lead to a thermodynamically favoured FM growth (e.g. for unfavourable formation of surfaces only existing at the islands or favourable formation of the inner film layers with respect to all other energies of formation) or SK growth (opposite cases).
In contrast if islands are formed directly on the substrate, - caused by the higher binding preference of the film material to itself – this is known as VW growth. The formation of thin flat films in this mode is not possible thermodynamically. However heating to high temperatures and fast cooling may result in flat films.
For evaporation of film material (e.g. Mg) so called Knudsen cells[10] can be used, consisting of a source material in a crucible, which are heated.

2.2. Low energy electron diffraction

LEED[11] is a method to determine periodic surface structures via diffraction of low energy (less than one keV) electrons. A possible experimental setup is shown in figure 2.1. Herein electrons are accelerated to a surface and the diffraction pattern is visualized on a fluorescent screen. This diffraction is based on the path difference of the electrons scattered on different lattice planes resulting either in constructive or destructive interference. The refraction angle θ between the incident beam and the diffracting lattice plane can be calculated by Braggs law of diffraction (equation 2.2).[12] Herein n is the order of diffraction, λ the wavelength of the electrons and d the distance of lattice planes.

$$n\,\lambda = 2d\,\sin(\theta) \tag{2.2}$$

The resulting diffraction pattern can be treated as a partial representation of momentum space. The momentum space – also called reciprocal space – is based on momentum as real space is based on length. The diffraction pattern can be used to calculate the lattice parameters, determine the surface symmetry and to identify superstructures at the surface.

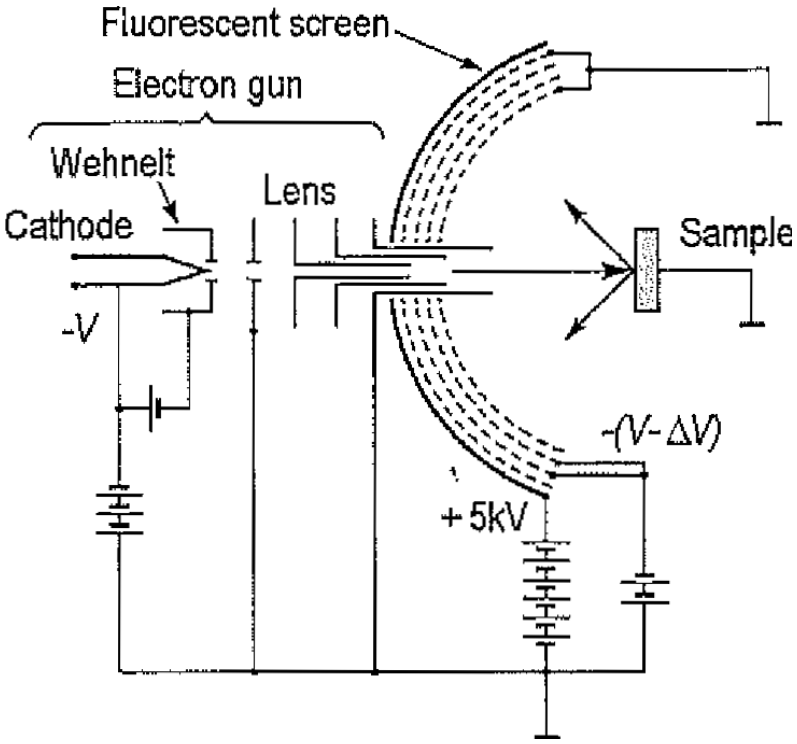

Figure 2.1: Basic setup of a four-grid reverse-view LEED.[9]

The low acceleration voltages result in a negligible probability for the electrons to reach more than the first few atomic layers of the sample. Therefore LEED is surface sensitive, but vacuum is required to avoid diffraction of electrons on residual gas atoms.[13]

Additionally peak intensities and the profile can partially be used to identify the surface unit cell content and to estimate the long range order.

For comparison to real space techniques one has to take into account the integrative character of LEED. Nevertheless according to Ref. [14] most surface structures have been solved quantitatively using LEED (see figure 2.2).

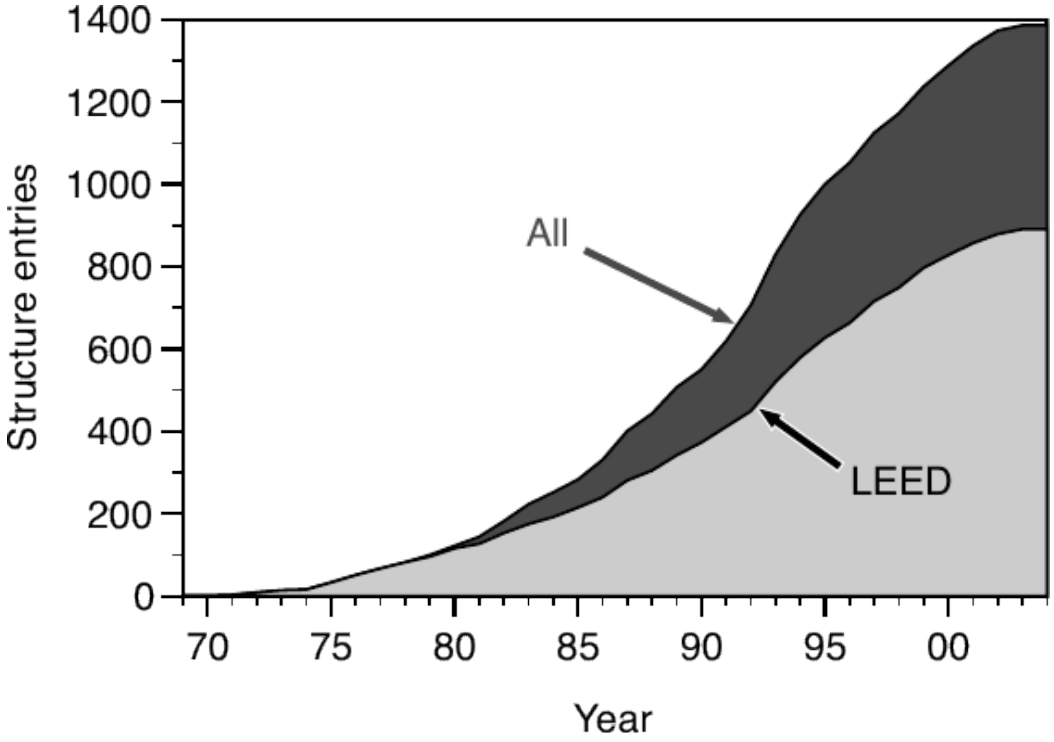

Figure 2.2: Dependency of solved structures on the method (only LEED and entirety shown) and the publications year according to the NIST surface structure database. Adopted from Ref. [14]

2.3. Auger-electron spectroscopy

In Auger-electron spectroscopy[15] the Auger-Meitner effect is used to investigate the elemental composition and chemical environment of surface atoms. The Auger-Meitner process is visualized in figure 2.3. Thereby an electron (ca. 20 - 3000 eV kinetic energy) can be used to excite a core electron to leave the atom. The latter one is called secondary electron. Its place is then filled by an outer shell electron. The energy that is released by this process can be used to excite a so called Auger-electron, which then leaves the atom, too.
For heavy elements the release of an X-ray photon instead is favoured.

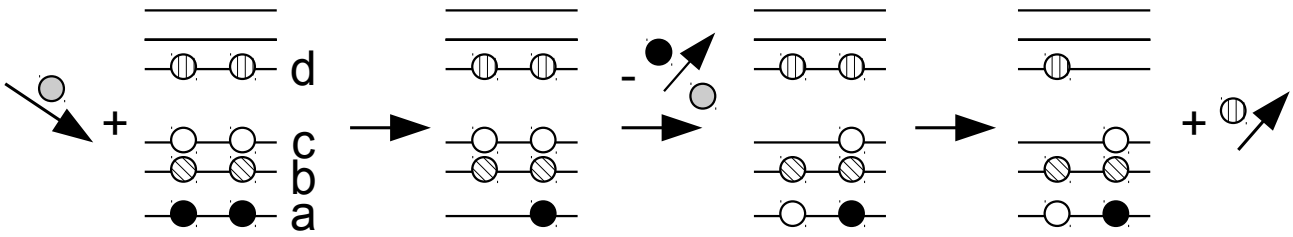

Figure 2.3: Chemist like notation of the Auger process: An initial electron (grey) is used to excite a core electron (black) at energy level (a), which leaves the atom. Then an outer shell electron (white) at energy level (c) fills its place and the energy difference is released by a so called Auger-electron (vertically striped) at energy level (d). The pattern on electrons is used to mark their original state, no properties shall be associated with it.

The Auger-electrons have specific kinetic energies corresponding to the energy difference of the relaxing electron and the energy necessary to release the Auger-electron (in figure 2.3 (a)-(c)). The transitions can be associated to the energy levels of the secondary electron, the relaxing one and the Auger-electron. In the approximation, that the ionization does not change the energy levels of the investigated atom, the kinetic energy of the Auger-electron E_{kin} can be expressed[16] as:

$$E_{kin} = E_a - E_c - E_d \tag{2.3}$$

Herein E_a, E_c and E_d are the energy levels of the secondary, the relaxed and the Auger-electron in the original atom state, respectively, as marked in figure 2.3.

Usually the transitions are named according to the shells of the involved electrons in the notation of the Bohr model. For example an O-$KL_{II}L_{II}$ transition is the process of generating a hole in the K-shell, which is filled by a L_{II}-shell electron. The released energy is used to excite another L_{II}-shell electron as the Auger-electron.

Experimentally this technique is challenging as the directly released electrons and the electrons used to excite them have to be separated from a small Auger-electron current.

For retarding field analysers like the one shown in figure 2.1 lock-in amplification is used during the detection scan of the Auger electrons kinetic energy. This technique uses a small oscillation overlayed by the linear energy sweep and a phase sensitive detection of this oscillation to improve the signal to noise ratio. As a result differentiated spectra are obtained.

As a convention the minimum peak of the transition is used to assign the kinetic energy to the transition. In this work assignment of peaks was carried out using data from Ref. [15].
The relatively low energies of the Auger-electrons make this technique surface sensitive, comparable to LEED. The results of both methods can be combined to allow both, the characterisation of structure and elemental composition for evaluation of surfaces.

2.4. Scanning tunnelling and non-contact atomic force microscopy

The used combined scanning tunnelling and non-contact atomic force microscope[7] is able to provide atomically resolved images of local surface areas. Thereby the current and the force signal can be measured at the same time, resulting in images that allow investigation of the surface morphology and its electronic structure.
Figure 2.4 shows the microscope's setup. It is situated in a UHV-chamber inside of a liquid helium bath cryostat. This cryostat is thermally coupled to the microscope via an exchange gas chamber.
To reduce external vibrations on the microscope different stages of vibrational isolation have been installed.
The microscope can be seen in figure 2.4 (II). It consists of a a portable sample setup (h) and a walker unit (a), that contains the sensor (e) and is moved by shear stack piezos (n). The walker unit is used to approach the microscope sensor to the surface of the sample (g). After approaching the tip to the sample surface the x and y piezos (b) can be used to move the sensor laterally on the surface, whereas the z piezo (c) is used to regulate the distance to the surface.
The nc-AFM/STM sensor is shown schematically in figure 2.4 (III). The conducting tip (Pt/Ir) is glued onto a tuning fork, to be electrically isolated but mechanically attached to it. The current modulated by the local density of states of the surface is measured via a µm wire. The frequency shift, corresponding to a repulsive or attractive force from the surface, is measured via the contacts T1 and T2 at the tuning fork. An excitation piezo is used to ensure a constant oscillation amplitude at varying frequencies.

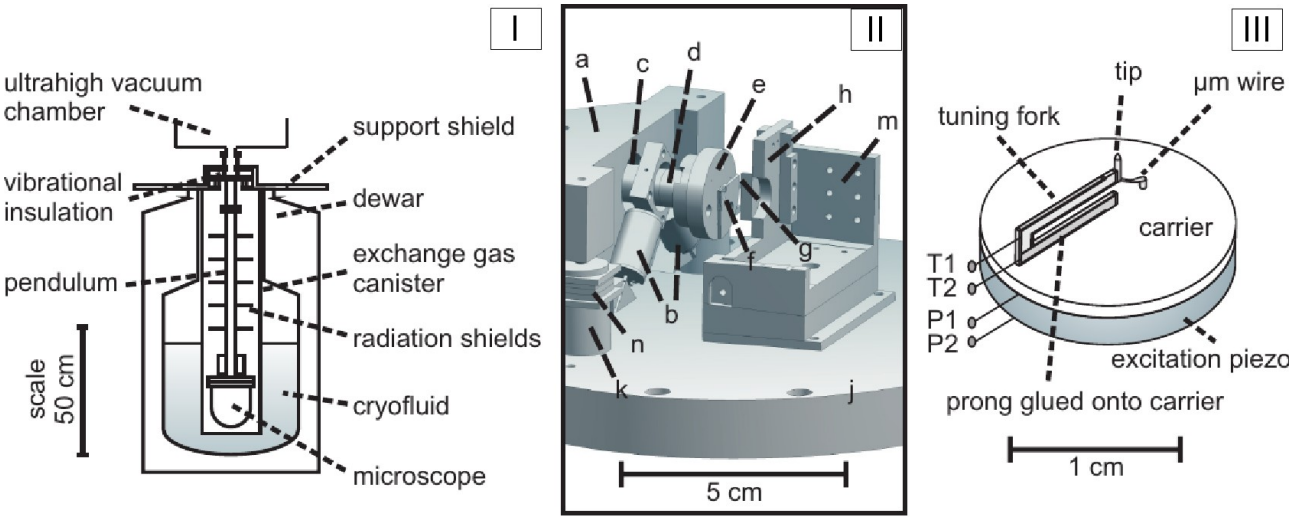

Figure 2.4: Setup of the custom-built nc-AFM/STM microscope, adopted from Ref.[5] (I) Schematic of an Eigler-style bath cryostat. (II) Schematic of the microscope on its support stage (a) walker unit, (b) x, y piezo and (c) z piezo of tripod scanner unit, (d) excitation piezo, (e) sensor carrier, (f) tuning fork assembly, (g) sample (cutted), (h) sample holder (cutted), (j) microscope stage, (k) walker support, (l) shear stack piezo and (m) sample stage (cutted). (III) Sensor setup. (P1) and (P2) contacts of excitation piezo, (T1) and (T2) contacts for nc-AFM signal of tuning fork.

The STM part of the detector offers the possibility for spectroscopic studies of the surface with respect to the tip.[17,18] One of these spectroscopies is scanning tunnelling spectroscopy (STS)[4], which is used to investigate the electronic states of the surface near the Fermi energy. For metals the Fermi energy is defined as the energy of the highest occupied electronic state at 0 K.

Another spectroscopic methods is field emission resonance (FER)[17,19], which uses electronic states in the vacuum to probe the surface. Thereby the work function of the system can be obtained. The work function describes how much energy is necessary to remove an electron from the surface material into the vacuum.

Using the combination of STM and nc-AFM the work function of surfaces can be determined indirectly via measurement of the contact potential differences (CPD).[5] Therefore the contact potential of the tip to the sample surface and to a known surface has to be measured and subsequent summation has to be applied. For the measurement of the contact potential the frequency shift during bias sweeping can be measured at constant height. At the lowest frequency shift the contact

potential of tip and surface is equilibrated, which defines the contact potential difference of the tip and the surface.

So with nc-AFM and STM and the resulting spectroscopies surfaces can be investigated locally with respect to their electronic structure and morphology. Furthermore it has been shown, that STM[20] and nc-AFM[21] can be used to acquire chemical sensitivity for the discrimination of chemical species like atoms or molecules.

2.5. Mass spectrometry and temperature programmed desorption

If a surface, where a gas is adsorbed, is heated, the gas can desorb with a probability dependent on the temperature, the heating rate and the gas species' binding energy to the surface. The resulting temperature programmed desorption[22–24] spectra obtained, when the amount of desorbing gas is plotted over the actual temperature can be analysed when heating is applied precisely linear. The amount of the desorbing gas can be determined via a pressure gauge or mass selectively by quadrupole MS.

Via mass spectrometry[25] one separates ionized particles according to their mass to charge ratio and measures the intensity in dependence of these ratios.

A mass spectrometer contains an ion source, an analyser, which separates the masses and a detector. Common mass spectrometer contain an ion source, which allows sample insertion at atmospheric pressure, whereas in UHV- apparatus it is used as a residual gas analyser, which ionizes molecules present at the gas phase.

A common analyser is a quadrupole. It consists of four parallel rods, that are used to form an electric field in their centre. The electric field contains a static and an oscillating part, which are chosen such, that only ions of a specific mass to charge ratio are able to reach the detector during a defined measuring time. Therefore a quadrupole mass selector can easily switch between different mass to charge ratios and thereby record TPD spectra of multiple desorbing species within one experiment.

As detectors Faraday cups or a secondary electron multipliers can be used. The former one is basically a metal cup at constant electric potential, at which the current flow is measured to, when

hit by ions. The latter one uses a secondary electron multiplier. Therefore even small intensities can be measured.

This functionality of a mass spectrometer allows the discrimination of the desorbing species and high signal to noise ratios. Therefore mass spectrometers are used as a detector in TPD. In the existing UHV-chamber a Balzers Prisma QME 200 is installed. For TPD experiments a new mass spectrometer (Hiden HAL 201) was ordered as higher sensitivity and scan rates during detection and more important a chemical inertness to the desorbing species is required.

Via Redhead analysis[22] (extension of reaction kinetics) TPD spectra can be used to assign activation energies to the desorbing species, estimating the reaction order. This information can be combined with other techniques to understand the reactions taking place on surfaces. This technique allows to run parts of chemical reactions in UHV.

On the model catalysts CO will be the probing molecule due to its many advantages.[2] It is not only used in the probably best known heterogeneously catalysed reaction – the CO oxidation – but plays a role in different other reactions like the water gas shift reaction or on many transition metals e.g. to $Ni(CO)_4$. Additionally, it has been shown that the CO desorption from bulk[26] and thin film[27] MgO exhibits multiple desorption maxima for CO adsorbed on defects and terrace sites. The thin film and bulk films exhibit different relative desorption intensities for these maxima.

Figure 2.5 shows the setup that is planned for the TPD experiments in side and top view. On the first picture the so called Feulner cup[28] (c) with a mass spectrometer inside (g) can be seen. This Feulner cup is used for a higher signal to noise ratio at the MS during experiment, which is realized by raising the pressure inside the cup. As a drawback of the Feulner cup the raise of readsorbing molecules has to be named. This leads to redesorbing molecules with partially wrong associated temperatures and if multiple gases desorb, different sticking coefficients may lead to complex analysis of the spectra. The pumping cross section at the back of the Feulner cup and the pumping performance are responsible for the pressure inside it. This pressure determines the prologation of the retention time at the mass spectrometer. Thereby the signal to noise ratio and the extension of the peak maxima are defined.

The heater (d) consists of a filament surrounded by a Wehnelt cylinder, which can be used for electron impact and radiative heating.

In the centre of both images the portable sample setup (a) can be seen, which will be described later (chapter 2.7). It is attached to a custom designed clamp (b), which is inside of a thermal shield (e).

A metallic ring (f) isolated from the Feulner cup is used to measure the distance to the sample capacitatively.

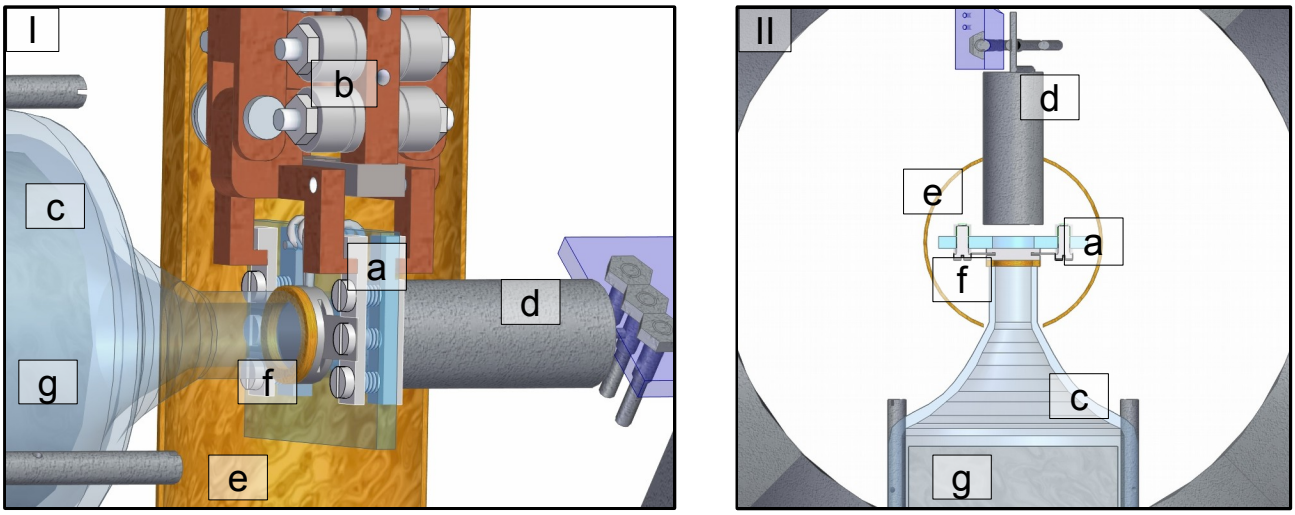

Figure 2.5: Side (I) and top view (II) of the TPD setup with partially cutted elements. (a) portable sample setup, (b) custom designed clamp, (c) glass Feulner cup, (d) heater (filament inside of Wehnelt), (e) thermal shield (cutted), (f) metallic ring for capacitative distance measurement, (g) mass spectrometer (inside Feulner cup).

2.6. Overview of existing setup

Figure 2.6 shows a scheme of the existing setup of the UHV-chamber system. It consists mainly of two parts: a main chamber (a), containing the microscope and a preparation chamber (c). In between is the gas supply unit (d), several shutter valves (g) and a Balzers Prisma QME 200 mass spectrometer (j). The connection pipe is also used by the horizontal manipulator (l) to transfer samples from one chamber into the other.

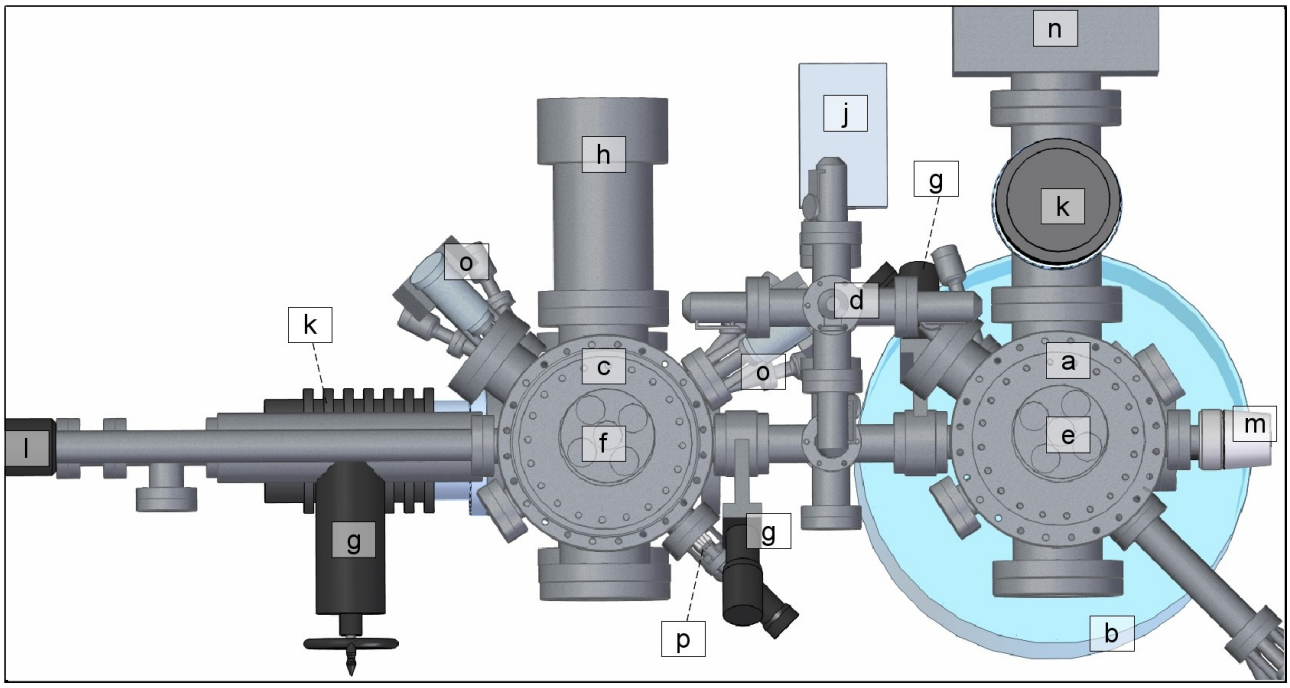

Figure 2.6: Top view of schematic draft of the UHV-chamber system.
(a) main chamber, (b) cryostat and nc-AFM/STM microscope within, (c) preparation chamber, (d) gas supply unit, (e) manipulator to microscope, (f) manipulator (to be replaced), (g) shutter valves, (h) LEED/AES analysis system, (j) mass spectrometer, (k) turbomolecular pumps, (l) horizontal transfer manipulator with sample garage underneath, (m) cold cathode pressure gauge, (n) ion getter pump, (o) triple evaporators, (p) sputter gun with heater setup underneath.

The main chamber contains the microscope (described in chapter 2.4) inside of a cryostat (b), a heating stage (nearly completely hidden by gas supply unit on the top left part of main chamber), pressure gauges (m), a turbomolecular (k) as well as an ion getter pump (n), an evaporator (outside of image) and the vertical manipulator (e), which can be used to transfer the portable samples down to the microscope.
The preparation chamber contains a Specs ERLEED 1000A LEED/AES analysis system (h), a sputter gun (p), a heater (underneath (p)), two Focus EVC 300 triple evaporators (o), a sample garage (underneath (l)), the vertical manipulator (l) and pressure gauges and pumps (e.g. (k)).
For the implementation of a TPD setup changes of the preparation chamber were planned and partially installed. (state: June 2013)

2.7. Portable sample setup

Figure 2.7 shows the portable sample setup. In its centre a single crystal (a) is mounted on a sapphire carrier (c) via molybdenum sheets (e) and slits (b). The sheets connect the sample mechanically and electrically to the grounding bars (g) that are screwed (f) together at the sides of the setup. These grounding bars are used to hold the portable sample setup within a clamp at the manipulator and to ground the sample. On top of the sample setup and at the single crystal thermocouple wires (d) are attached to measure the sample temperature. In the back the sapphire carrier has a hole, which allows heating of the single crystal but is not shown here.
For the Mo(001) sample a setup in a molybdenum frame (figure 2.7 (III)) was used earlier. During this thesis the Mo(001) samples were attached to a sapphire plate like in figure 2.7 (II).

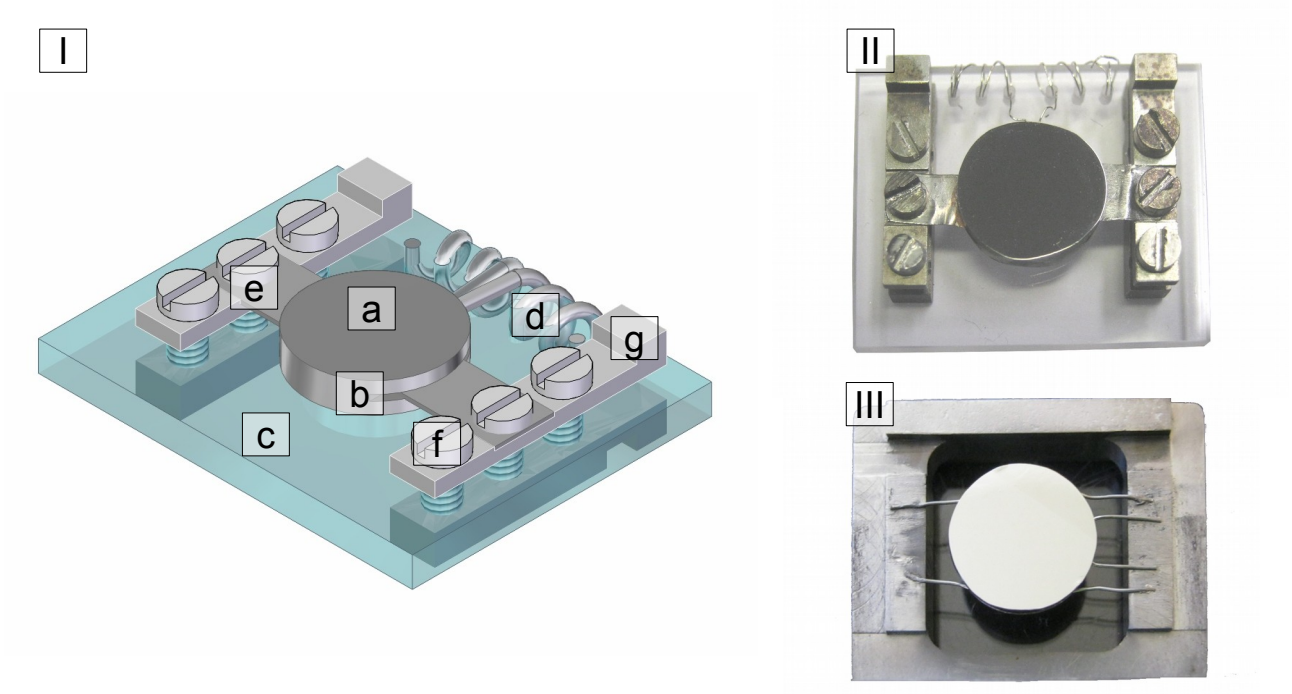

Figure 2.7: (I) Drawing of the portable sample setup. (a) single crystal sample, (b) slits for attachment, (c) sapphire carrier, (d) thermocouple wires, (e) molybdenum sheets, (f) screws for attachment of (g) grounding bars. (II) Photograph of the Fe(001) portable sample setup (III) Mo(001) portable sample setup in a molybdenum frame.

2.8. Changes in existing setup

To perform TPD experiments the previously described UHV-chamber system (see chapter 2.6) has to be modified. The TPD setup was planned to be implemented in a flange cross underneath the preparation chamber. Additionally a cross for pressure gauges was installed and the existing manipulator has to be substituted.

The actual and planned setup for the TPD experiments is shown in figures 2.8 and 2.9. The former one shows a photograph of the actual state (June 2013) and a top view cut through the TPD experimental area, whereas the latter one shows a side view cut through the preparation chamber with the new TPD stage underneath. Within this stage a turbomolecular pump (a), a mass spectrometer (b), a heater (c) and a view port (d) were mounted. Leak valves (e), the Feulner cup (f) and the thermal shield around the sample (g) have not yet been implemented.

In the following chapters special features and requirements of the implementations will be discussed.

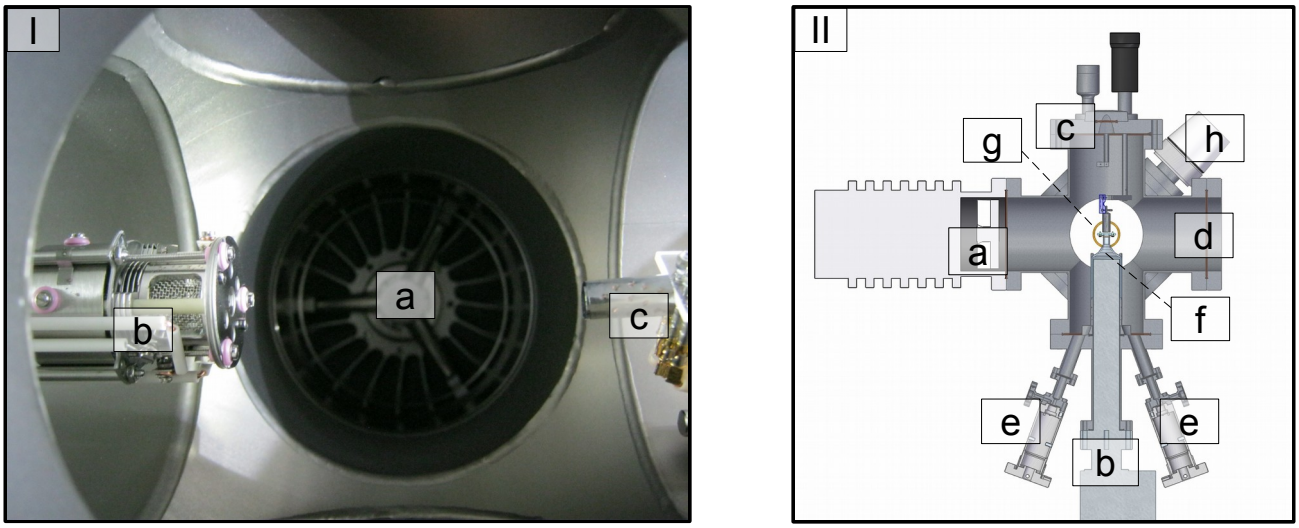

Figure 2.8: Photograph (I) of the actual state (June 2013) and planned TPD setup draft (II). (a) turbomolecular pump, (b) mass spectrometer, (c) heater, (d) view port (used to take image (I)), (e) leak valves for gas insertion, (f) Feulner cup, (g) thermal shield around sample and (h) cold cathode pressure gauge.

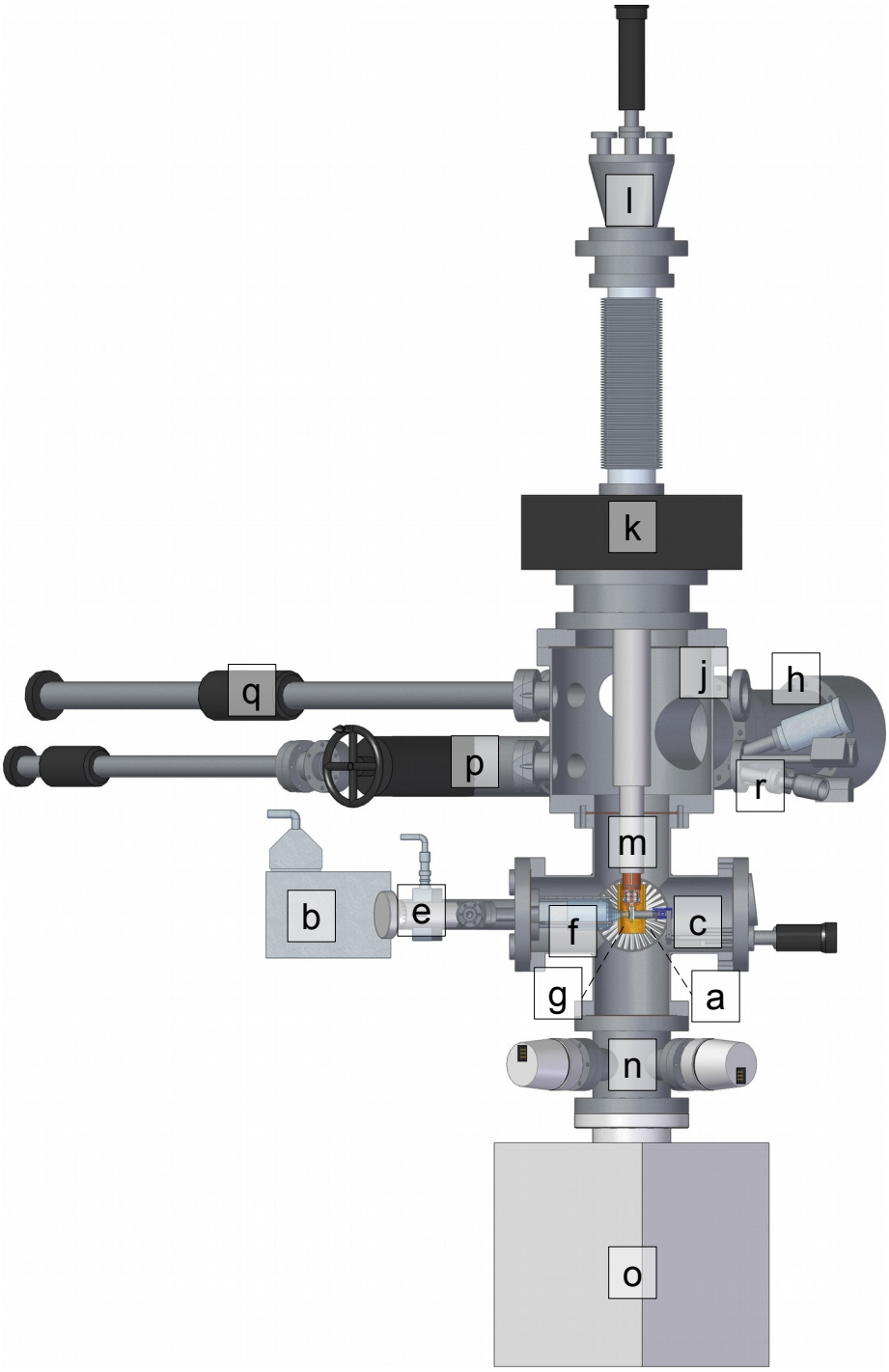

Figure 2.9: Cut through planned preparation chamber setup. (a) turbomolecular pump, (b) mass spectrometer, (c) heater, (e) leak valve, (f) Feulner cup, (g) thermal shield around sample, (h) LEED/AES analysis system, (j) flange for transfer to main chamber and microscope ,(k) x- and y-positioning of TPD manipulator, (l) manipulator head, (m) manipulator cooling unit, (n) cross flange with pressure gauges, (o) ion getter pump, (p) sample garage with shutter, (q) horizontal manipulator for transfer to microscope and (r) triple evaporator.

2.9. Manipulator requirements

Due to the low temperatures required in TPD experiments of CO on MgO[26,29] a custom-built liquid helium cooled manipulator has to be implemented. The current manipulator is used to establish electrical contact to the thermocouple wires of the portable sample setup and to transfer it into the sample carrier, the LEED/AES analysis system and the vertical transfer manipulator. Additionally it must mechanically fix the sample in its position and ensure electrical connection to an outside connector. This connector should not be connected with chamber ground to measure current from the sample during electron impact heating, LEED/AES and sputtering.
The new manipulator is required to provide the same functionality, but furthermore cool the sample to a temperature of about 20 K. This will be achieved via a liquid helium flow cooling, and coupling via heat exchange to the sample. Therefore the mechanical contacts to the portable sample setup should provide a high contact surface and high contact force. This shall be provided by a custom made clamp, as shown in figure 2.5 (b). This clamp is custom-built at the FHI workshop according to Solid Edge drawing made in the AFM group.
Additionally, a thermal shield for screening the sample from thermal radiation of the surrounding UHV-chamber system needs to be implemented. The shield was designed to move vertically with respect to the manipulator to allow LEED/AES measurements.
A manipulator fulfilling these requirements was specified and ordered during the processing time of this thesis.

2.10. Heater requirements

A photograph of the implemented heater can be seen in figure 2.10. It was designed according to a previously existing electron impact heater. With a transfer rod (e) one can extend and retract a filament and the Wehnelt cylinder (a) surrounding it. Therefore the filament can be moved into heating position and retracted afterwards. The adaption of the existing setup allows the use of existing equipment.

A view port (b) was added to this heater setup to monitor the sample approach. According to Ref. [23] high precision of distance measurement in this area is necessary to provide reproducible TPD spectra.

The heater has to be regulated via an external heater controller (HS 170, Schlichting Physikalische Instrumente, 82205 Gilching), which will be called here Schlichting controller. It uses a PID feedback loop, which will be described in the experimental part, chapter 3.1. There also the consistency of the heating behaviour measured with linear temperature ramps will be presented.

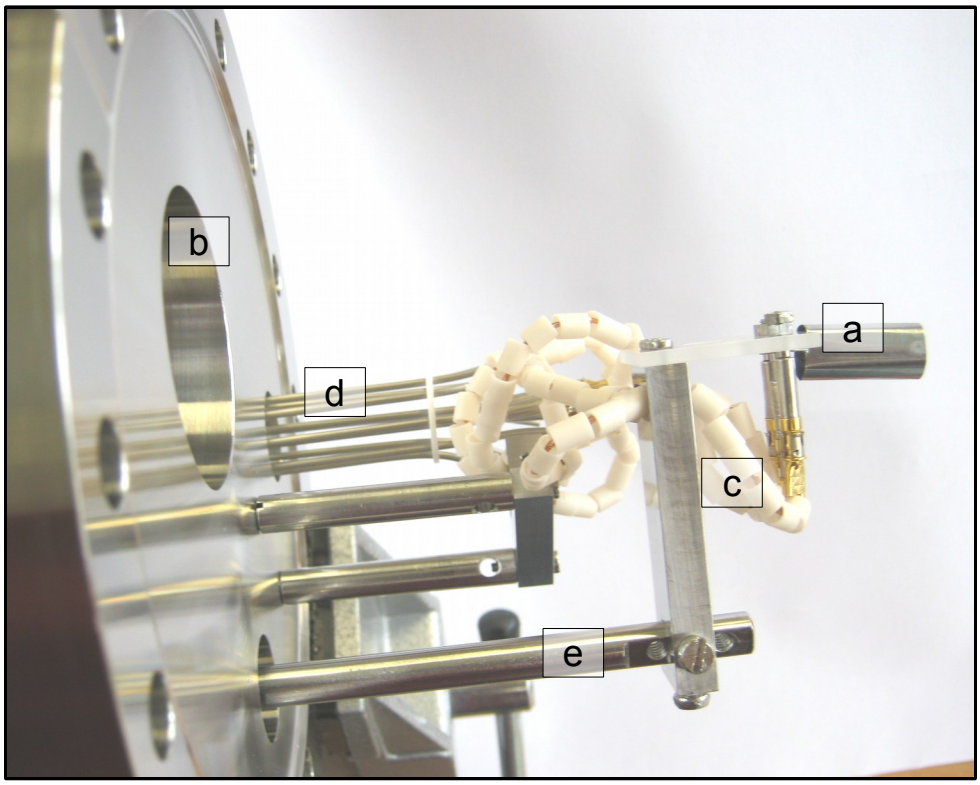

Figure 2.10: Photograph of implemented heater. (a) Wehnelt cylinder with filament inside, (b) view port, (c) Cu wires for filament and Wehnelt, (d) electrical feedthrough, (e) transfer rod

2.11. Mass spectrometer and Feulner cup

To measure the amount of desorbing gas molecules and to characterise these the usage of a mass spectrometer is one of the common approaches. The usage of a so called Feulner cup was shown[30]

to be able to raise the signal to noise ratio in TPD of single species. This Feulner cup is an enclosure around the measurement sensor, which is used to exclude desorbing species from the outside of the investigation area, reduce interference from other parts of the UHV-chamber system and raise the partial pressure close to the mass spectrometer.[23] Its disadvantage is readsorption, which causes some of the desorbed species to readsorb and redesorb with a time delay. Due to the temperature ramp used in TPD this time delay leads to a assignment of a higher desorption temperature to these twice desorbed species.

For higher signal to noise ratios the wall surface of the Feulner cup nozzle and the distance to the sample surface have to be minimized and the Feulner cup material has to be chosen such, that the probing molecules have low sticking coefficients with its surface.[23]

In our case the distance measurement shall be done capacitatively, via a small copper ring attached to the front of the Feulner cup with the sample as a counter electrode[23]. This ring shall be coated with gold, to lower its chemical reactivity.

The Feulner cup (a) itself was decided to be made from glass and can be seen in the photograph of the Feulner cup assembly in figure 2.11. (The ring for capacitive distance measurement is still absent, state: June 2013.) The springs (c) are used to keep the Feulner cup in its position, while reducing the contact pressure of the supporting rods (b) at single points of the glass. The small holes in the supporting rods shall be used for cables and gas tubing fixation too. The supporting flange (d) was custom built to provide access for gas lines and electrical feedthroughs.

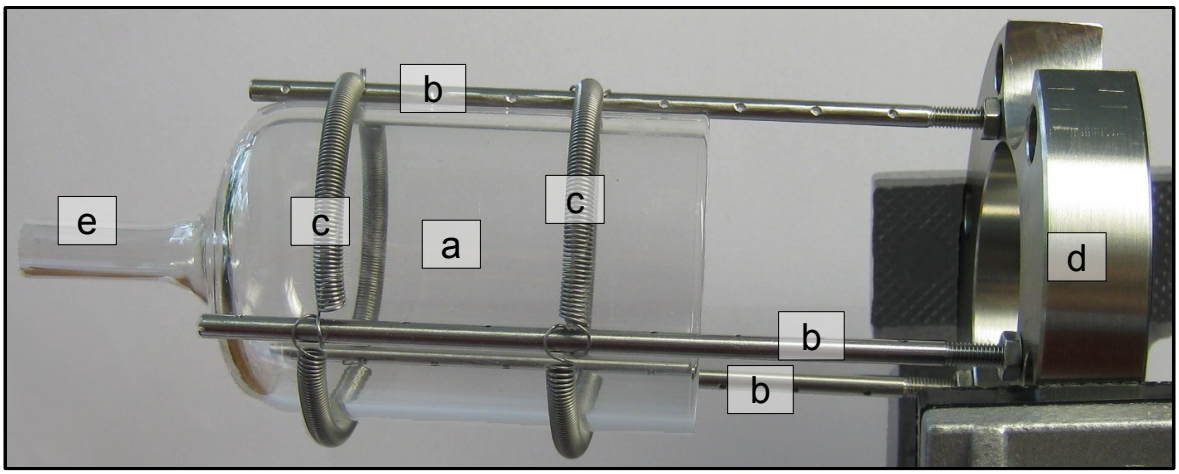

Figure 2.11: Photograph of Feulner cup assembly. (a) Feulner cup, (b) supporting rods with holes for cables and (c) springs, (d) supporting flange, (e) nozzle (without metallic ring for capacitative distance measuring) to insert in thermal shield (see figure 2.5).

3. Results and discussion

The focus of this thesis' research project was to implement a temperature programmed desorption setup into the existing UHV-chamber system for the investigation of model catalysts. The used model catalysts are MgO films deposited on metal single crystals (see chapter 1).
Earlier investigations of these model catalysts have been carried out in the Chemical Physics department of the Fritz-Haber-Institute using either Ag(001) or Mo(001) as supporting material. On Ag(001) for low coverage of MgO no flat films have been observed, that exhibit an exclusively MgO covered surface.[8] This limits investigations of doping effects of MgO as in thin films the substrate may have a severe influence on the film[3,4] and dopants might segregate into the substrate. An occurrence of silver islands may influence in integrative investigations like TPD.
The Mo(001) single crystal was attached to a molybdenum frame due to the high annealing temperature when cleaning Mo(001) or after MgO deposition. The usage of a molybdenum frame for Mo(001) has been observed to be adversely in comparison to a sapphire carrier with respect to temperature measurements. (Due to an incompatiblity of thermocouples with the molybdenum frame temperature measurements were carried out with a pyrometer.) Therefore cleaning of Mo(001) when attached to a sapphire carrier and Fe(001) as a substrate for MgO deposition were investigated. Fe allows a higher annealing temperature than Ag, and requires a lower one than Mo, which may allow thicker MgO films and support by a sapphire carrier, respectively. The lattice constant mismatch of Fe(001) and bulk MgO lies in between of those of MgO and either Ag(001) or Mo(001).
In the following section of this thesis the implementation of the TPD setup will be discussed as well as the experiments that have been carried out. Furthermore literature data of the model catalysts will be presented and related to the results obtained during this thesis.

3.1. Implementation of TPD setup and evaluation of heater setup

In an existing UHV-chamber system containing a high resolution scanning probe microscope performing nc-AFM and STM, a TPD setup was partially implemented. Beforehand threedimensional models of the new setup where created using Solid Edge (CAD program by

Siemens PLM software), which were used to produce the pictures seen in the theoretical part. This was necessary to evaluate general spacial options and for drawing of technical drafts (see attachment). These technical drafts were used to produce the necessary UHV-parts in the workshop of the Fritz-Haber-Institut. After production, cleaning and assembling these parts were implemented into the UHV chamber.

In the next step the precise requirements of the cryostat manipulator were discussed, and it was discussed which company could fulfil the requirements best. Afterwards the necessary apparatuses and equipment were ordered at Cryovac.

To test the necessary heater power a model setup in another vacuum chamber was installed. It consisted of a portable sample setup, which is cooled passively and a heater regulated by a temperature controller. A scheme of the setup is visualized by figure 3.1. A computer is used as the interface for programming the regulation controller (Schlichting). The output signal of the latter is used to control a power supply (ES 030-5, Delta Elektronika, Netherlands), which is connected to the heater filament inside vacuum to heat the sample. At the sample a thermocouple (either type K or C) is or will be attached, which is used for the Schlichting controllers PID feedback loop, named after its proportional, integral and differential part.

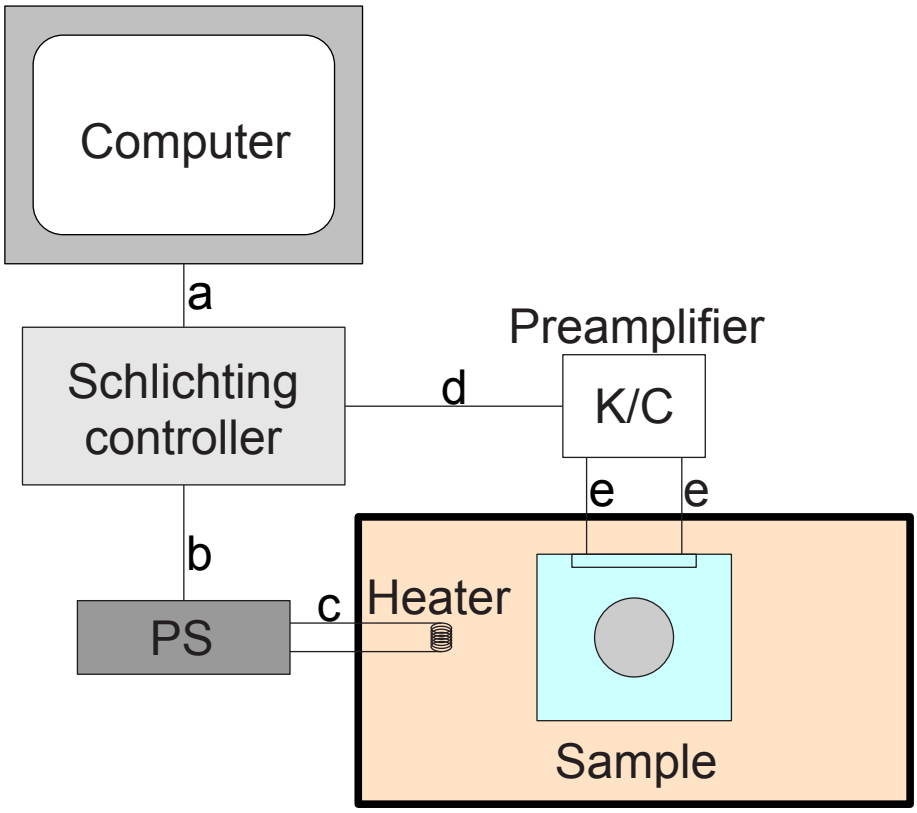

Figure 3.1: Scheme of heating model setup (bold line resembles UHV-chamber borders), (a) RS 232 data connection, (b) BNC – 9-Pin D-Sub analogue programming signal, (c) filament heating wires, (d) connection to preamplifier of either type K or C, (e) thermocouple wires, (Schlichting) temperature feedback controller, (PS) power supply (ES 030-5, Delta Elektronika, Netherlands),(K/C) thermocouple preamplifier.

The feedback loop uses three parts to regulate the output power $P_{heating}$, according to equation 3.1, but limits $P_{heating}$ to a value between zero and one hundred percent of the defined maximum output power.

$$P_{heating} = P_{prop} + P_{int} + P_{diff} \tag{3.1}$$

The three addends are calculated by the actual temperature $T_{prevailing}$ and the set point temperature T_{set} according to equations 3.2, 3.3 and 3.4. c_{prop}, c_{int} and c_{diff} are the proportionality constants, that have to be set manually and t is the time since starting the experiment.

$$P_{prop} = c_{prop} \cdot (T_{set} - T_{prevailing}) \tag{3.2}$$

The proportional part alone cannot reach the set temperature.

$$P_{int} = c_{int} \cdot \sum_{t=0}^{now} T_{set}(t) - T_{prevailing}(t) \tag{3.3}$$

The integral part allows reaching the set temperature, but is much slower than the proportional part, when applied alone. Together both parts are sufficient to be used as a PI feedback loop.

$$P_{diff} = c_{diff} \cdot \frac{\partial (T_{set} - T_{prevailing})}{\partial t} \tag{3.4}$$

The differential part is the derivation of the differences, which allows to avoid spikes in the temperature curve, as it reacts to rapid changes in the measured temperature, but cannot be used alone.

To obtain the proportionality constants for the PID feedback loop, they are at first all set to zero. Afterwards the feedback controller is used in P mode setting to heat to a fixed T_{set}, raising successively only c_{prop} until the temperature oscillates around a constant value. Then c_{prop} is reduced to about 60% of that value. Next a PI feedback loop is used with the same fixed T_{set} raising successively only c_{int} until the temperature oscillates around T_{set}. Now c_{int} is reduced to about 70% of that value. Afterwards c_{diff} can be found using the same procedure PID feedback loop controlled, keeping c_{prop} and c_{int} constant and reducing the found c_{diff} to about 40% of the oscillation value.[31]

According to Redhead[22] within a TPD experiment temperature ramps can either be applied linearly or reciprocally (meaning an exponent of plus or minus one for temperature over time, respectively). Due to the high mechanical stress when heating reciprocally (very fast temperature change in the beginning) a linear temperature ramp was chosen. An example for the ramp is shown in figure 3.2. The experiment behind this figure was carried out from a point near room temperature (340 K) using a constant heating rate of 0.5 K/s to 440 K. As visible in figure 3.2 the set and actual temperature do only differ in a sub K range, while the output power is raised without abrupt

changes and oscillations. The spikes in the difference of set point and sample temperature could be associated with a rapid cooling of the chamber when moving the entrance door.

The distance dependence of the heater filament to the sample was investigated within a range of several millimetres. No significant deviations of the temperature curve in figure 3.2 (upper part) were found. The necessary output power during this was found to change slightly, raising if the heater was retracted and vice versa.

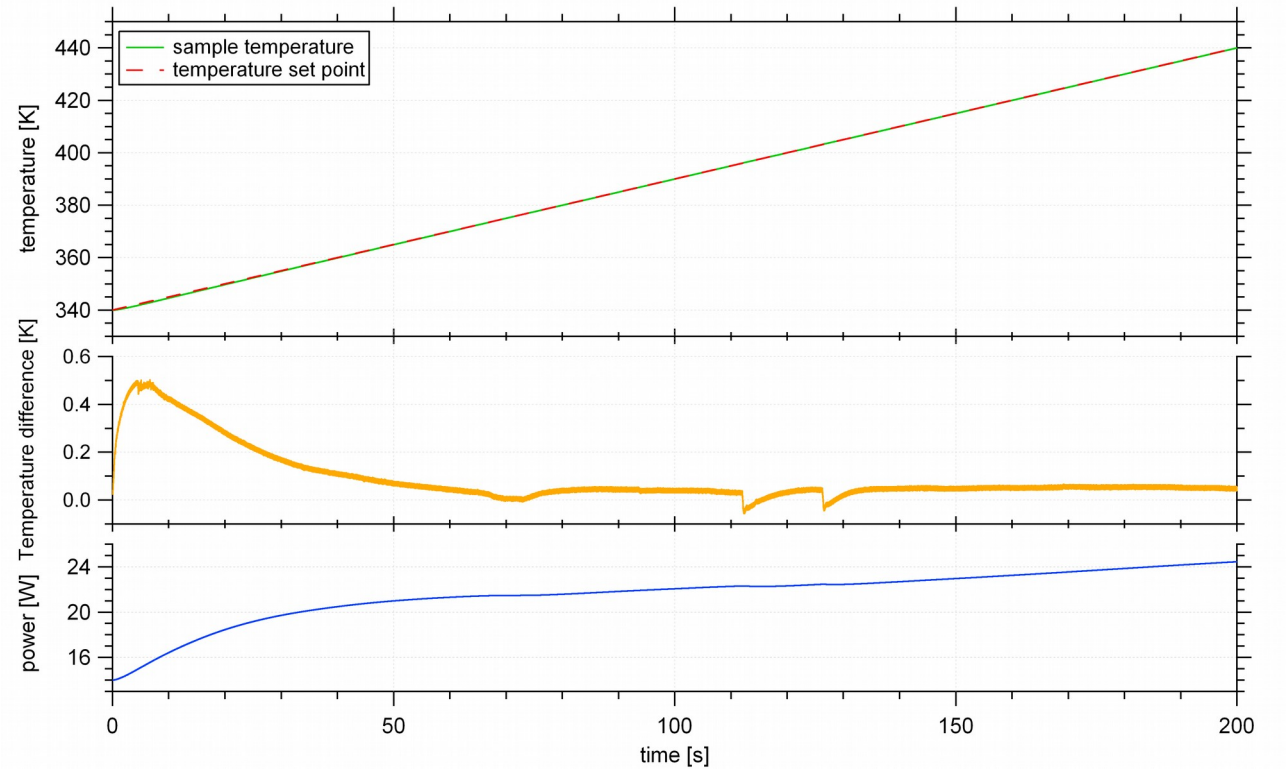

Figure 3.2: Programmed heating profile and resulting temperature, difference between both as well as output power of heater during radiative heating of a NiAl(110) reference sample.

3.2. Preceding investigations of model catalysts

This chapter shall give a short introduction to the literature data available to the model catalysts shown in figure 1.1, consisting of MgO films on different metal substrates. Some properties of these

systems, namely MgO films on Ag(001)[4,18,32–35], Fe(001)[4,36–42] or Mo(001)[4,35,43–45] substrates have been investigated intensively. STM-images of two monolayer thick MgO films on these metal supports are shown in figure 3.3.

Thin MgO films grow epitaxially on the mentioned metal substrates and are due to different bulk lattice parameters strained or compressed. Assuming the bulk MgO bond length as a reference, one can calculate the deviation of the metal substrate bond length to it and interpret this as an expression for the stress existing in thin MgO films on metal substrates. Thereby one obtains a deviation of 3.1 % for MgO on Ag(001), 3.9 % on Fe(001) and -5.4 % on Mo(001). The latter one is expressed negative to indicate support lattice parameters exceeding the MgO ones. These values have been calculated according to the length of the metal surface lattice, taking into account the growth directions of the MgO films (MgO[100] || Ag[100], MgO[110] || Fe[100], MgO[110] || Mo[100]) as described in literature cited in the beginning of this chapter.

The effects of the raising magnitude of lattice differences can be seen in figure 3.3. In the case of silver flat terraces, for iron small cavities and for molybdenum a moire like pattern can be observed. This indicates a strong influence of the metal substrates on thin MgO films.

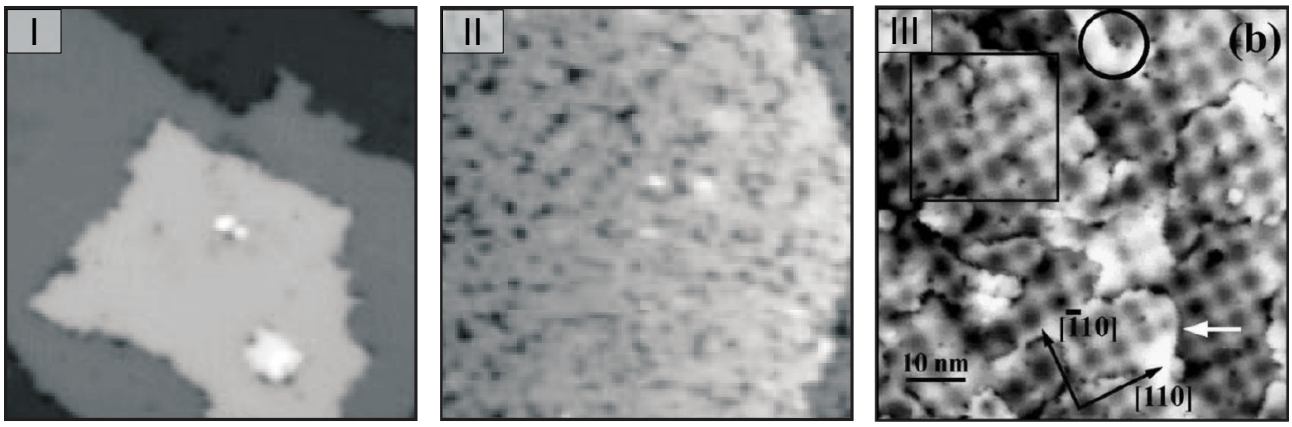

Figure 3.3: 70 x 70 nm² STM images of two monolayer thick MgO films on different metal substrates taken at bias voltages of about 3 V in constant current mode; (I) Ag(001)[4], (II) Fe(001)[40] and (III) Mo(001)[44].

Additionally to the morphological features of the MgO films on single metal crystals electronic effects may be present that influence the chemical behaviour of the model catalysts.[3,4,46] Doping experiments of magnesium films have also been carried out, showing a change in structure with respect to the pristine case.[45]

Studies on Mo(001) investigated the strain and its release of MgO films due to annealing.[44] They have shown that strain reduces with higher annealing temperatures and is also reduced when growing thicker films.

Another interesting feature of MgO films is the growth behaviour itself. On Ag(001) studies have been carried out showing a difference in the polarity of edges, probably dependent on the preparation method. Thereby either polar[32,34] (only Mg or O at the borders, along the bulk MgO [110] and [$\bar{1}$10] directions) or non-polar[33] (MgO borders, along the [100] and [010] directions) edges have been observed. The amount of edges showing a different polarity than the majority was negligible in each case. All samples exhibited film coverages of 0.3 - 2 monolayers generated by evaporation of Mg in a O_2 atmosphere. Differences may be found in the Mg evaporation rate (not fully given), the O_2 pressure (ranging from $2 \cdot 10^{-8}$ to 10^{-6} hPa) or slight variations of the substrate temperature (470 K to 500 K) during MgO growth.

On Fe(001) non-polar edges have been observed.[47] These edges are referred to misfit dislocations of the MgO layer with the iron substrate and films were 8 ML thick. STM-images of another reference[48] suggest the existence of polar edges, but are difficult to assign exactly, due to a lack of resolution.

Preparation methods of MgO on Fe(001) have been investigated intensively.[41,42,49–51] A reason for this is the Fe/MgO/Fe system, which is expected to exhibit giant magnetoresistance properties[37], which can be used among other things in the sensors for electronic data storage. Under O_2 rich conditions the system contains an FeO layer between the MgO and the bulk Fe(001), which is said to be the reason for an unexpected change in the magnetoresistance properties.[50] For O_2 poor conditions a debate is ongoing about the absence or existence of the FeO layer.[41,49]

As we want to study model catalysts these properties are not the main interest of the research project, nevertheless the knowledge on the preparation of MgO films on Fe(001) was used.

In the literature mainly two different types of preparations are known. On the one hand the evaporation of MgO and deposition onto the Fe(001) substrate[37–42] and on the other hand the evaporation of Mg in a O_2 atmosphere.[50] Although the former one is used more often (probably due

to its simplicity) the latter one was investigated intensively according to its growth conditions effects. Thereby the deposition of Mg and post oxidation and annealing[48] was investigated, as well as the dependence on the deposition rates of O_2 and Mg, their ratio and the substrate temperature during the latter depostition.[47] The authors come to the conclusion that growth conditions of about 0.1 nm/min of MgO at about 10^{-7} hPa O_2 pressure at temperatures ranging from room temperature to 570 K and subsequent annealing result in most balanced growth conditions. "Most balanced" means neither substrate oxidation, nor oxygen deficiency in the oxide film, nor undefined interface layers. Both references[47,48] do not agree whether to deposit magnesium during O_2 exposure or to post-oxidize it.

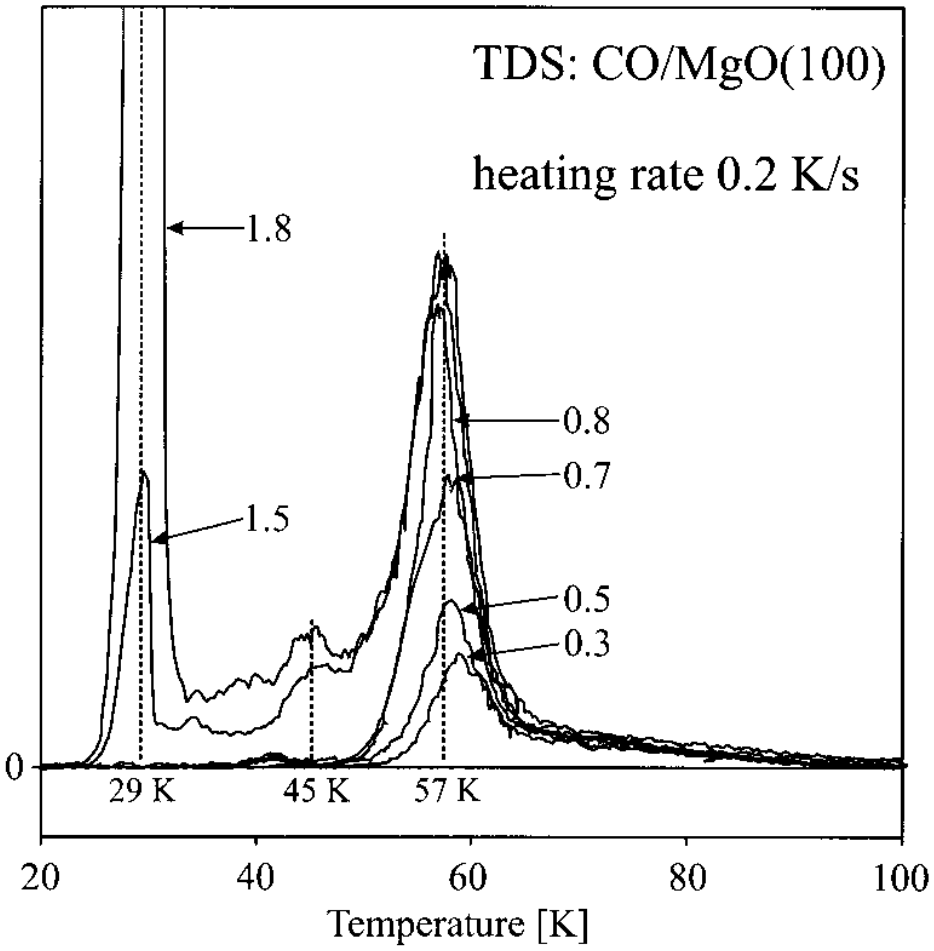

Figure 3.4: Temperature programmed desorption spectra of CO deposited on bulk MgO.[26] The numbers indicate the fraction of CO monolayer coverages at the start of the TPD experiments.

Temperature programmed desorption experiments of CO have been carried out on bulk[26] and thin films[27,29] (on a Mo(001) substrate) MgO. Both show a desorption maximum at a temperature of about 57 K. The thin film spectra show additional maxima at elevated temperatures. The 57 K maxima were associated with desorption from terrace sites, the latter ones to the desorption from defect sites, like low coordinated Mg atoms.[29] An example for a TPD spectra on bulk MgO can be seen in figure 3.4.[26] The additional peak at 29 K was associated with multilayer desorption of CO.

In conclusion many investigations of the model catalysts (see figure 1.1) have been carried out. LEED, AES, STM, nc-AFM as well as other techniques have been applied at least to some of the systems. As the MgO/Fe(001) interface is part of a special magnetoresistance property device the preparation methods of MgO on Fe(001) have been investigated intensively.

MgO films have been shown to exhibit either polar or non-polar step edges. MgO films on Mo(001) have been observed to release strain upon annealing or further films deposition.

TPD of CO has been applied to MgO films on Mo(001) showing defect associated desorption not found on bulk MgO.

The aim to combine reactivity studies with investigations of the morphology and the electronic structure may complement the existing studies and gain deeper insight in mechanisms involved in catalysis on oxide films.

3.3. Cleaning procedures

This chapter will present the results of cleaning procedures of pristine Mo(001) on sapphire carriers and pristine Fe(001). These cleaning procedure, carried out in UHV are necessary for the growth of defined MgO films on metal single crystals. The cleanliness of the substrate shall prevent the influence of small amounts of other elements, which could persist as dopants, on the MgO films. Higher amounts of contaminants can also influence the surface morphology, which can be monitored by LEED and/or AES. Usually these cleaning methods consist of a combination of sputtering, heating, annealing, oxygen treatment and/or treatment with reductive gases.[52,53]

For the cleaning of Mo(001) single crystals the most abundant pollutants known are sulphur and carbon.[52] For Fe(001) the main contaminants are carbon, sulphur, oxygen, nitrogen, phosphorus and chlorine.[52]

Cleaning of molybdenum has been carried out by different methods (see [52,53]). One, which will be called tempering procedure here, is the combination of one hour argon sputtering at 10^{-5} hPa with 1.5 kV acceleration voltage and tempering for 10 min at about 1500 K. Another one is the combination of the same sputtering with a flashing step, during which the sample is heated to 2100 K for 30 s. In both cases a rate of temperature change of about 3 K/s with electron impact heating was used.

A comparison of the two cleaning methods is necessary to evaluate whether cleaning of Mo(001) can be carried out at lower temperatures, that allow usage of a sapphire carrier. Therefore both procedures were applied after oxidizing the sample in an O_2 atmosphere (10^{-6} hPa at 1400 K for 30 min). For comparable testing a procedure was carried out twice, LEED images were taken and the sample was reoxidized. During flashing and tempering steps oxygen desorption intensity (m/c = 16) was investigated via MS. The intensity integrals of both procedures were comparable, whereas the tempering procedure had a lower desorption rate. Desorption kinetics stayed constant, except when the temperature was increased or reduced.

LEED patterns taken at 75 eV electron energy of Mo(001) cleaned with both procedures are shown in figure 3.5. Both LEED patterns exhibit the expected (1x1) diffraction peaks. The flashed sample (figure 3.5(b)) shows lines between the diffraction spots, which were not visible by eye. These lines could represent many small spots aligned with lower intensity than visible by eye and therefore stand for a high order superlattice or could be present due to an imaging error. The LEED pattern of the tempered Mo(001) (figure 3.5(a)) shows diffraction peaks with small satellites around one spot (in $[\bar{1}00]$ direction, other spot intensity may be to low). Low energy electron diffractograms of different electron energies (55, 60, 90, 105, 120 eV) have been taken and show the same trend. Therefore it was concluded that both procedures show comparable cleaning of the Mo(001), that may be sufficient for deposition of thick MgO films. Nevertheless for a more qualitative comparison further investigations like AES have to be applied.

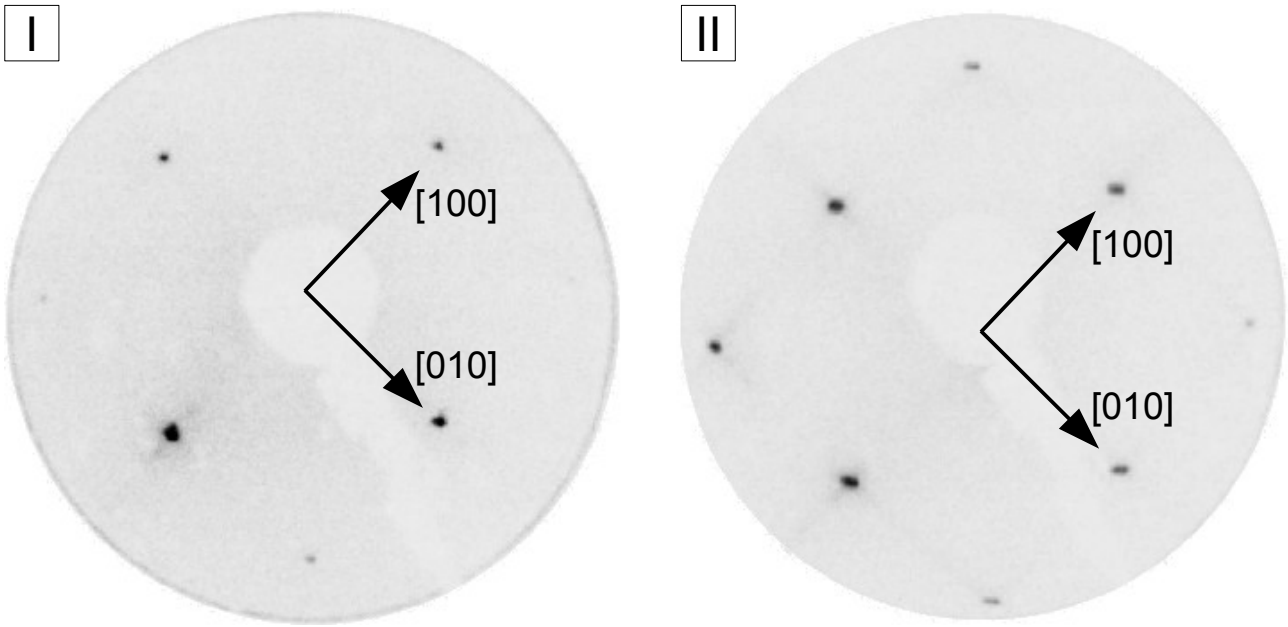

Figure 3.5: LEED images at 75 eV of differently cleaned Mo(001), (I) twice sputtering and tempering, (II) twice sputtering and flashing (description of methods in text).

In comparison to Mo(001), Fe(001) has a broader variety of contaminants and cannot be heated above 1183 K.[53] At this temperature iron transforms from its body centred cubic structure into its face centred cubic modification. To prevent sulphur segregation to the Fe(001) surface annealing procedures have to be carried out at temperatures higher than 700 K, according to Ref. [52].

The applied cleaning procedure consists of argon sputtering at elevated temperature (approx. 800 K, 10^{-6} hPa, 14.5 h) and at room temperature (20 min) followed by annealing at 720 K for 1 min with passive cooling. Afterwards LEED and AES were carried out, resulting in the diffraction pattern and the spectra shown in figure 3.6 and 3.7. The diffraction pattern shows a c(2x2) superlattice at 90 eV acceleration energy.

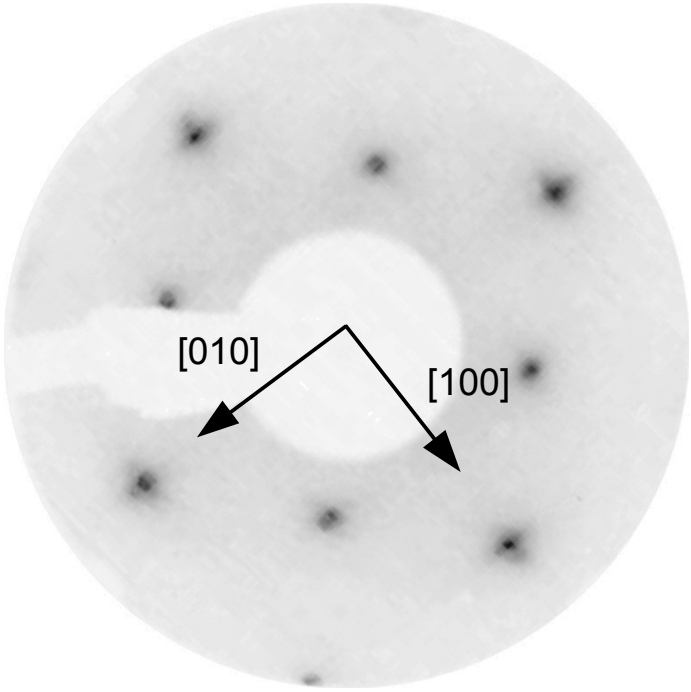

Figure 3.6: LEED images of cleaned Fe(001) taken at 90 eV electron energy

AES was carried out using an electron acceleration voltage of 3 kV and lock-in amplification. It showed strong peaks at kinetic energies of about 600 eV, 650 eV and 700 eV corresponding to the Fe $L_{III}M_{II;III}M_{II;III}$, $L_{III}M_{II;III}M_{IV;V}$ and $L_{III}M_{IV;V}M_{IV;V}$ transitions, respectively. Also the weaker Fe $L_{II}M_{I}M_{I}$ and $L_{III}M_{II}M_{II;III}$ transitions at 550 and 560 eV can be found. At about 288 eV a peak probably corresponding to the C $KL_{II}L_{II}$ transition can be found.

Transitions corresponding to oxygen (490 eV for O $KL_{I}L_{II}$ and 515 eV for O $KL_{II}L_{II}$) and nitrogen (380 eV for N $KL_{II}L_{II}$) cannot be found. Transitions of phosphorus (120 eV for P $L_{III}M_{II;III}M_{II;III}$), sulphur (150 eV for S $L_{III}M_{II;III}M_{II;III}$) and chlorine (180 eV for Cl $L_{III}M_{II;III}M_{II;III}$) cannot be distinguished sufficiently from the background.

Due to this results the superlattice was assigned to be an indication for a carbon c(2x2) covered Fe(001) surface morphology, that was observed in literature before.[54]

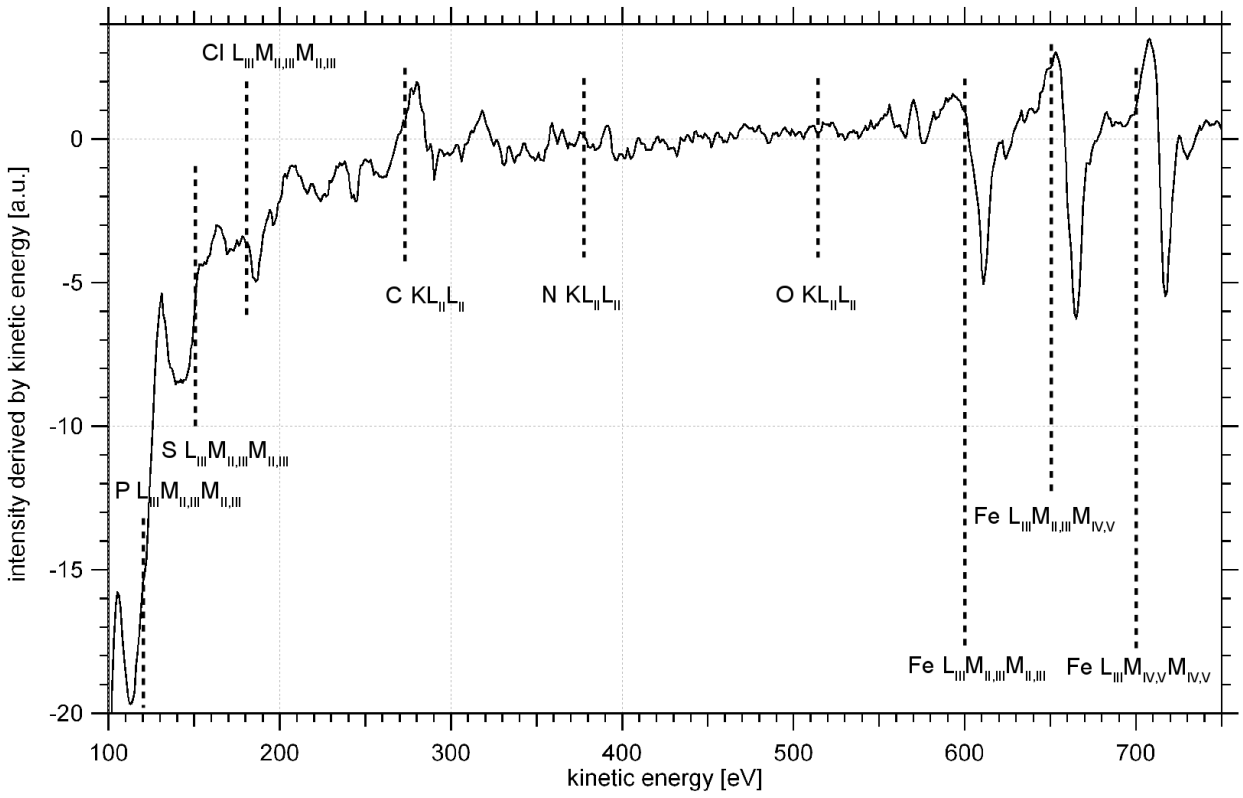

Figure 3.7: AES of cleaned pristine Fe(001), taken at 3 keV electron energy

The resulting STM-images in figure 3.8 show sharp, but not aligned or linear step edges (a) with multiples step heights of 143 pm corresponding to a Fe(001) surface structure. Also adsorbates (around (d)), subsurface contaminations (near (b)) and screw dislocations (c) can be observed. Due to cleaning problems no contaminant free Fe(001) surface was achieved. However, it was chosen to try the MgO film growth at the presented substrate quality.

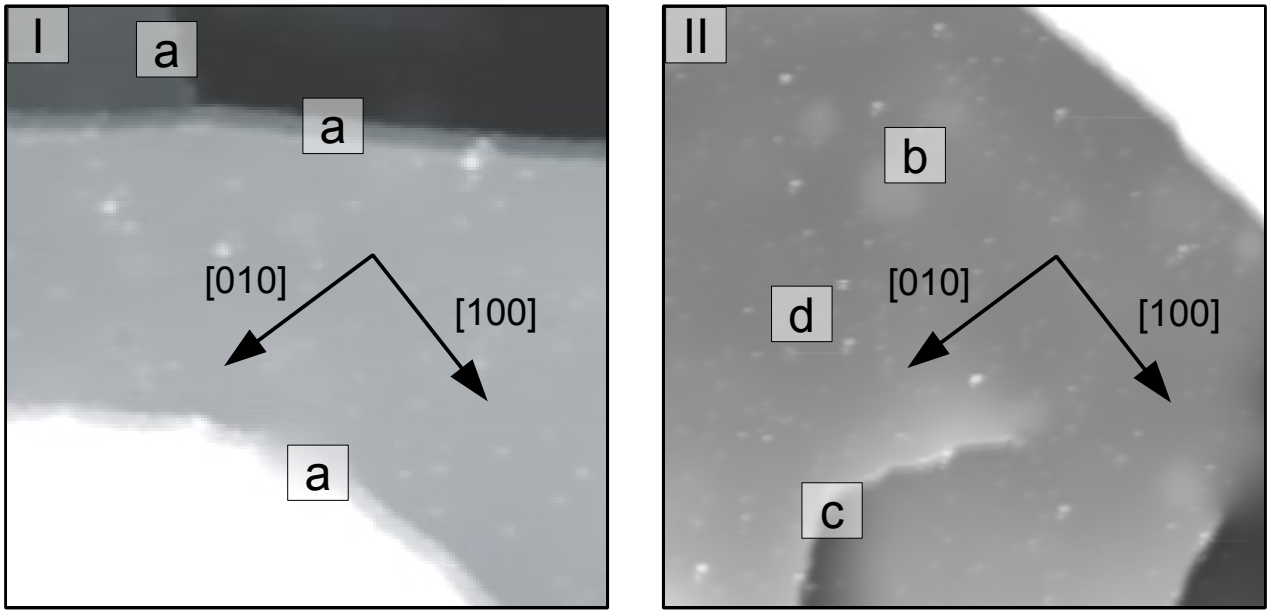

Figure 3.8: STM images of cleaned Fe(001), exhibiting a c(2x2) superstructure in LEED, taken at constant tunnelling current of 100 pA, bias voltage of 0.5 V and temperature of 78 K, (I) 40x40 nm^2, (II) 70x70 nm^2,
(a) step edges, (b) subsurface contaminations, (c) screw dislocation, (d) adsorbates.

3.4. Results of investigations of MgO deposited onto Fe(001)

After cleaning of the Fe(001) surface, it was exposed to MgO film growth conditions. Therefore Mg was evaporated from a Knudsen cell in O_2 atmosphere ($1 \cdot 10^{-7}$ hPa) for 7.5 min at a nominal Mg deposition rate of 0.09 nm/min. This corresponds to three monolayers of MgO, assuming an equal number of Mg atoms per unit area in MgO and Mg. Afterwards the sample was annealed at 720 K for 10 min.

The LEED pattern (see figure 3.9) shows distinct differences compared to the pattern of the pristine substrate (figure 3.6). Diffraction spots in [110] and [1$\bar{1}$0] directions, which belong to the c(2x2) superlattice of carbon are not present anymore.

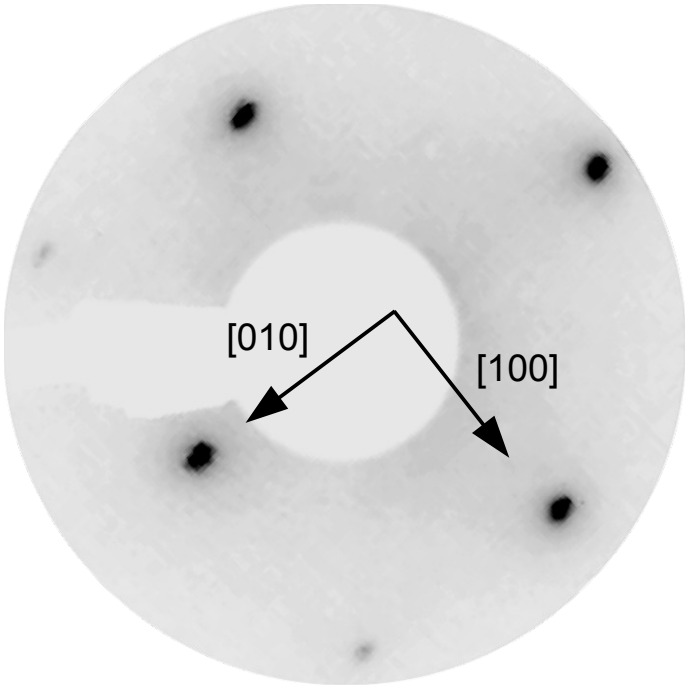

Figure 3.9: LEED images of MgO deposited on Fe(001) taken at 90 eV electron energy

AES results (figure 3.10) show a shift of the Fe $L_{III}M_{II;III}M_{II;III}$, $L_{III},M_{II;III}M_{IV;V}$ and $L_{III}M_{IV;V}M_{IV;V}$ transitions to slightly lower kinetic energies of the Auger electrons. This probably corresponds to shift in kinetic energy by a sensing error. An oxygen peak can be observed at about 515 eV corresponding to the O $KL_{II}L_{II}$ transition. No evidence for other usual contaminants (carbon, sulphur etc) of Fe(001) is given by AES.

From the LEED and AES of the coated Fe(001) one cannot conclude, whether the a formation of MgO films on Fe(001) was successful. But as the underlying substrate could not be identified as a clean Fe(001) without any superstructures, the formation of the film may have been influenced by the c(2x2) superstructure.

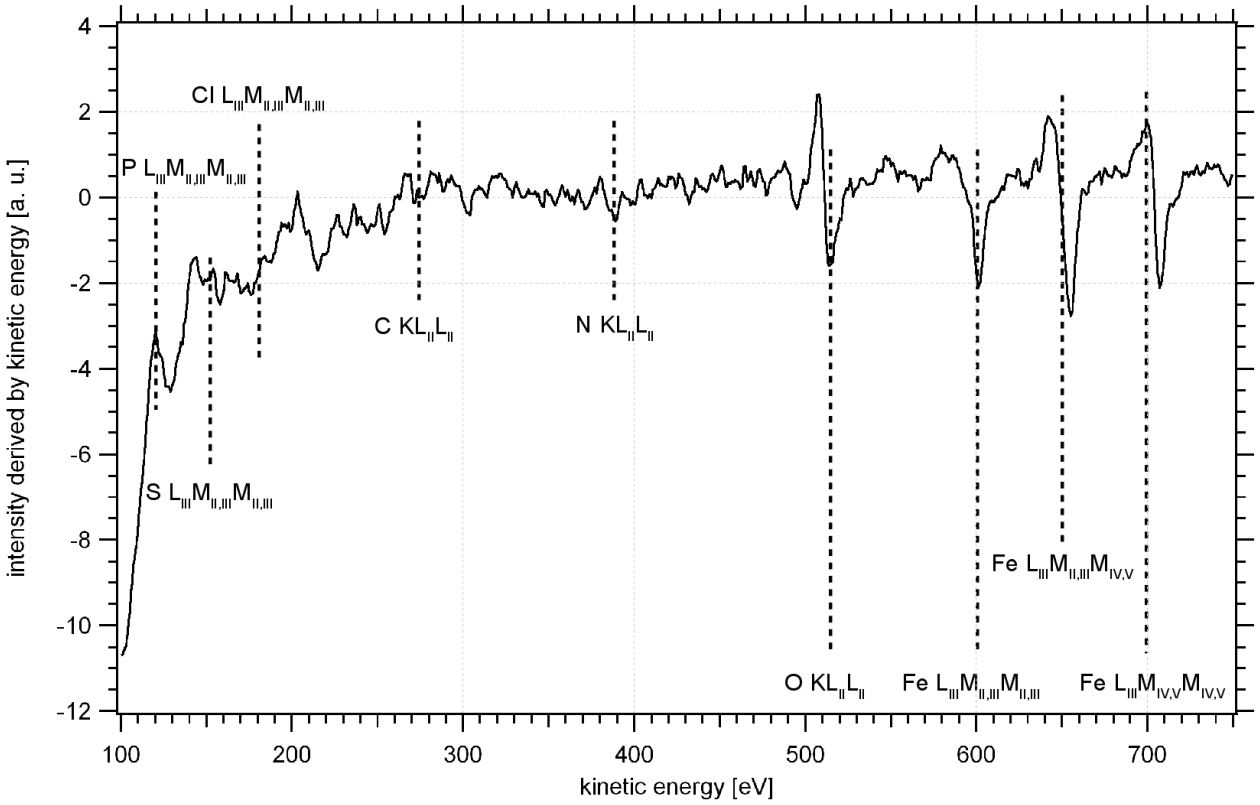

Figure 3.10: AES of MgO deposited on Fe(001), taken at 3 keV electron energy

In figure 3.11 STM images of the model catalyst can be seen. On the first view one can identify brighter patches (b) on a darker substrate (a). Measurements of the tunnelling current and frequency

shift as a function of the distance between the tip and the sample show that the bright patches exhibit oxide behaviour and the substrate has a metallic conductivity. This oxide behaviour means a delayed set in of current relative to the force signal, when approaching the tip to the surface, referenced to the metallic substrate.

In all the images the oxide patches exhibit well aligned edges. The polarity of them will be discussed at the atomically resolved images.

The amount of deposited MgO should correspond to a total substrate coverage of three monolayers MgO. In the STM images formation of island seems to have been preferred over large terrace growth as there are large sections of substrate and island that partially exhibit step heights of 4 nm, which would correspond to about 20 steps.

Step height analysis shows variances in the step height differences. They may be caused by the different conductivities of the oxide patches and the metallic substrate, or due to the existing C c(2x2) superstructure on the Fe(001) substrate. Nevertheless step heights are multiples of 0.4 nm, which would correspond to two layers of MgO, but the error is in the range of 0.1 nm.

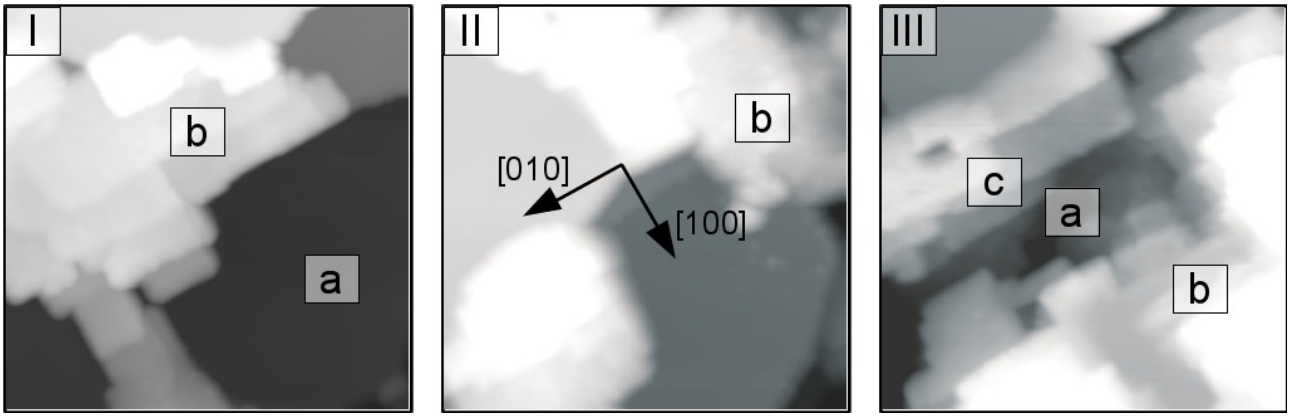

Figure 3.11: STM images of MgO deposited on Fe(001) taken at constant tunnelling current of 100 pA. (I-III) 70x70 nm^2, bias: 3.5 V; (given substrate lattice orientations are valid for (I-III)) (a) dark metallic substrate, (b) multiple step island patches, (c) tilted terrace.

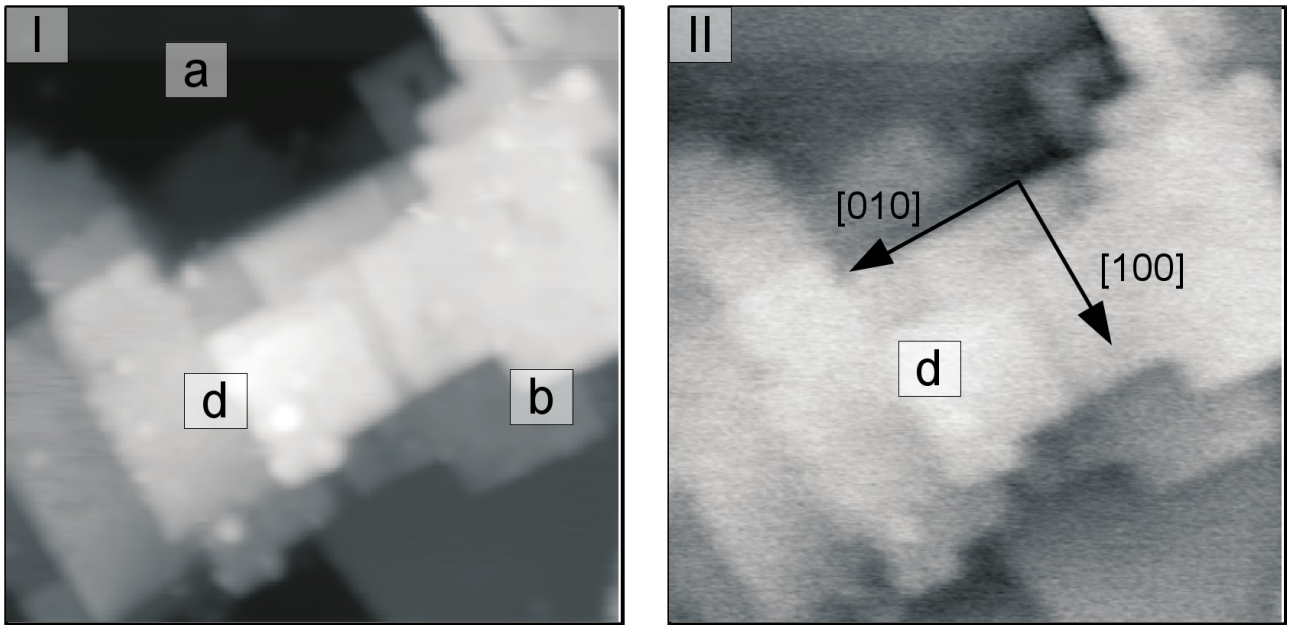

Figure 3.12: STM and nc-AFM images (50x50 nm^2) taken after MgO deposited on Fe(001).
(I) STM image taken at constant tunnelling current of 100 pA, , bias: 4.5 V,
(II) nc-AFM signal obtained during (I); df ≈1 Hz (excitation frequency shift);
(a) dark metallic substrate, (b) multiple step island patches, (d) possible defects.

The nc-AFM studies lead to the images shown in figure 3.12 and 3.13. Image 3.12 (II) resembles the force signal detected during constant current scan of image 3.11 (I). Both images together can be used to distinguish between electronic and morphologic effects. For example in the oxide pattern (b) small bright spots (d) can be identified that lead to a retreat of the tip, but did hardly influence the nc-AFM signal. This may be charge trapping defects on the oxide film, but an exact assignment is not possible here, due to missing spectroscopic studies.

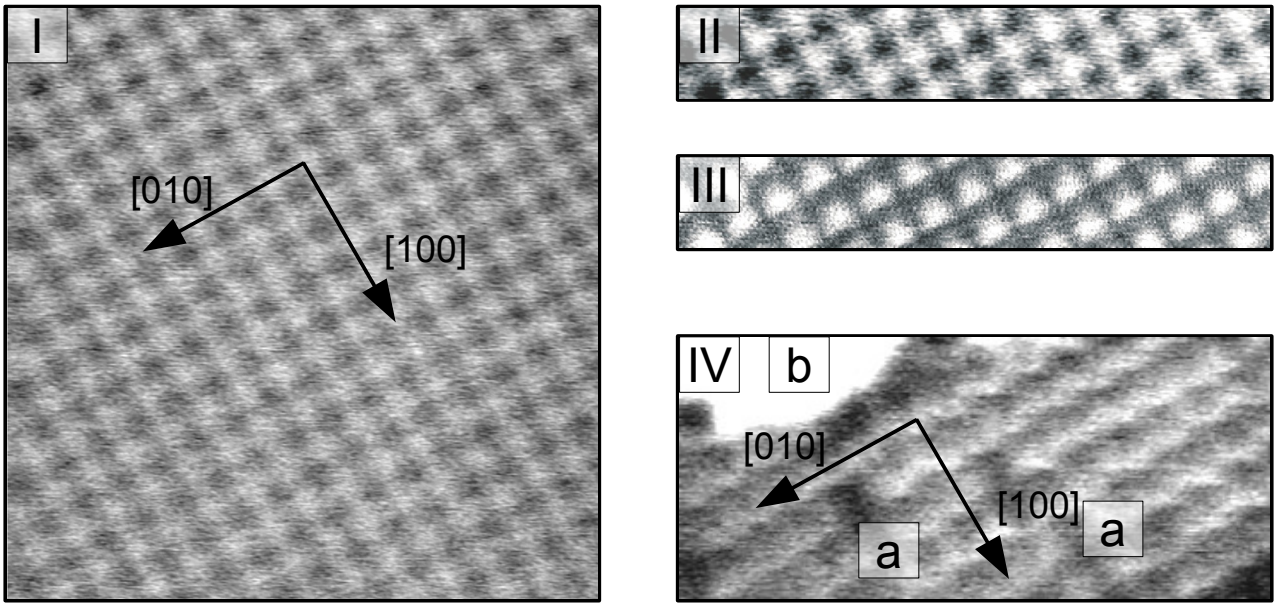

Figure 3.13: nc-AFM images taken after MgO deposition on Fe(001); (I) constant height (c.h.) image of the substrate, 4x4 nm², bias: 0.05 V; df ≈-4 Hz; (II) c.h. image of the substrate, 4x0.6 nm², bias: 0.05 V; df ≈-4 Hz; (III) STM image corresponding to image (II), tunnelling current ≈4 nA; (IV) c.h. image of the oxide film, 4x1.8 nm², bias: 0.05 V; df ≈-2 Hz, (orientations refer to substrate), (a) defects in oxide film, (b) elevation ends measurable area.

Image 3.13 (I) and (II) show nc-AFM images of the metallic substrate. They exhibit a clear square surface lattice, that can be associated with either Fe(001) or an (1x1) superstructure of oxygen, whereas the latter case is suggested by literature.[55] The measured surface lattice constant (0.29 nm) is in both directions exactly as expected in literature (0.29 nm[55]). The images 3.13 (II) and 3.13 (III) show a constant height image of the substrate and the corresponding tunnelling current, respectively.

Investigations of the oxide patches resulted in many images without atomic resolution or identifiable structures. One of the few obtained atomic resolution images is 3.13 (IV). It shows some defects (I) and elevations (II) of non atomic heights. Within the undistorted part a lattice constant of about 0.32 nm could be found, which is slightly higher than both, the substrate one (0.29 nm) and the expected one in bulk MgO (0.30 nm[56]). This may be due to a higher error due to the few measured atoms or caused by defects. The influence of the oxide structure by a probable underlying iron oxide cannot be excluded. This kind of oxidation could have changed the substrate morphology strongly, but would probably not result in larger substrate parameters, that could have

strained the oxide, as all commonly observed iron oxide species exhibit smaller nearest neighbor distances for the iron species (FeO: 0.30 nm[57],Fe_3O_4: 0.30 nm[58], Fe_2O_3: 0.26-0.30 nm[59]) than the observed oxide patches (0.32 nm). Nevertheless the observed atoms of the oxide patch exhibit nearly the same lattice and orientation as the substrate. If the oxide film would be MgO this epitaxial growth behaviour would be in agreement with literature.[41,42]

The orientation of the step edges of the oxide patches are along the Fe(001) [100] and [010] directions. This means that if the oxide patches would be MgO, all observed edges would be polar (so in MgO [110] and [$\bar{1}$10] directions). This is in contrast to recently observed MgO patches on Fe(001).[47] If not influenced by the superstructure exhibited by the substrate during deposition this difference in polarity of the edges of a potential MgO could only be assigned to the annealing temperature, as this differs significantly from preparation conditions described in literature.[47,48] In contrast to the assumption of flatter MgO structures on Fe(001) with higher annealing temperature[44,47] annealing with 720 K could have been at too high temperatures. Probably iron could have segregated into the oxide film. Investigation on iron diffusion into MgO films descibe a temperature range of about 620 to 870 K, where neither iron diffusion can be excluded, nor could be observed.[38]

4. Conclusions

This thesis showed the preliminary work on the model catalysts for the combination of reactivity experiments with investigations of the morphology and electronic structure. The model catalysts of the research project consist of a metal substrate (either Ag(001), Fe(001) or Mo(001)) coated with pristine or doped MgO films, as visualized in figure 1.1.
During the working time the implementation of a new temperature programmed desorption experimental setup was planned and partially completed. The parts, that were not implemented could not be finished within the working time, but are ordered and specified detailed at external enterprises and workshops.
Investigations of the model catalysts via combined nc-AFM and STM as well as with LEED and AES have been carried out.

The implementation of the temperature programmed desorption setup required the threedimensional drawing of the existing chamber setup and of the new parts, that had to be built. Experiments on the heating of a comparable sample providing linear temperature ramps have been carried out.
The investigations of the model catalysts included a comparison of different cleaning procedures of Mo(001) single crystals on a sapphire carrier for later usage as a substrate for thick, doped MgO films, evaluation of diffraction, spectroscopy and microscopy results on cleaned and MgO coated Fe(001). The latter ones showed a Fe(001) lattice like substrate, with a c(2x2) superstructure of probably carbon, which segregated from the bulk metal. On these substrates Mg was deposited in a O_2 atmosphere resulting in oxide islands on a metallic substrate. The oxide patches might consist of the former substrate superstructure C underneath as well as of Mg, O and/or Fe. Some properties of the oxide films show similar behaviour as reported about MgO films on Fe(001) like well oriented step edges all along the investigated area, and a comparable lattice constant. Other properties differ from literature data, like the orientation of these step edges. If the substrates superstructure was not responsible for resulting in this kind of oxide film, it may be due to a too high annealing temperature.
The investigations of doped thick MgO films on a metal substrate require either a further investigation in the cleaning methods of Fe(001) and the deposition methods or the usage of the investigated Mo(001) cleaning methods. The lower temperature cleaning method (tempering) has

been shown to be able to provide LEED diffraction pattern, that could allow deposition of thick MgO films, that can be investigated further on a sapphire carrier.

For the future the implementation of the ordered cryostat manipulator and the completed Feulner cup have to be done to be able to run temperature programmed desorption experiments of CO on the model catalysts.

If the investigation of morphology and electronic structure of MgO films on Fe(001) would be continued these studies would allow a further comparison of the substrate influence on the MgO films. Perhaps a similar effect for the different polarity of step edges dependent on the preparation conditions as on Ag(001) could be found on Fe(001) and further investigated.

5. Acknowledgement

First I would like to thank Prof. Freund and Prof. Risse for giving me the opportunity to do my thesis at the Fritz-Haber-Institute of the Max-Planck-Society as well as in the chemistry department of the Freie Universität Berlin.

For his great help and supervision I want to thank Dr. Markus Heyde.

For many explanations, measurements on the Fe(001) crystal, lots of helpful advices when proofreading and the huge amount of strained nerves I want to thank Stefanie Stuckenholz, who is currently working on the project to finish the setup and further investigating model catalysts.

Furher gratitude goes to Prof. Risse and Markus Heyde for proofreading of this thesis.

I want to thank again Prof. Freund for funding the visit of the Deutsche Physikalische Gesellschaft Spring Meeting of the Condensed Matter Section.

Also I want to thank Christin Büchner and Gero Thielsch for their help during this thesis.

In the end I want to thank the whole working group, all chemical physics department and organisational staff members for the nice working atmosphere, many cakes, cookies and interesting talks.

6. Literature

[1] G. Ertl, *Reactions at Solid Surfaces*, Wiley, **2010**.

[2] H.-J. Freund, G. Meijer, M. Scheffler, R. Schlögl, M. Wolf, *Angewandte Chemie* **2011**, *123*, 10242–10275.

[3] L. Giordano, G. Pacchioni, *Accounts of chemical research* **2011**, *44*, 1244–52.

[4] S. Schintke, W.-D. Schneider, *Journal of Physics: Condensed Matter* **2004**, *16*, R49–R81.

[5] T. König, G. H. Simon, L. Heinke, L. Lichtenstein, M. Heyde, *Beilstein journal of nanotechnology* **2011**, *2*, 1–14.

[6] G. H. Simon, T. König, H.-P. Rust, M. V. Ganduglia-Pirovano, J. Sauer, M. Heyde, H.-J. Freund, *Physical Review B* **2010**, *81*, 073411.

[7] M. Heyde, M. Kulawik, H.-P. Rust, H.-J. Freund, *Review of Scientific Instruments* **2004**, *75*, 2446.

[8] *Group Knowledge in the Catalysis, AFM and Magnetic Resonance Group of the Chemical Physics Department of the FHI Berlin*, **2013**.

[9] K. Oura, V. G. Lifshits, A. A. Saranin, A. V. Zotov, M. Katayama., *Surface Science - An Introduction*, Springer, Berlin, **2003**.

[10] M. Knudsen, *Annalen der Physik* **1909**, *334*, 179–193.

[11] J. B. Pendry, *Low Energy Electron Diffraction: The Theory and Its Application to Determination of Surface Structure*, Academic Press, **1974**.

[12] C. Gerthsen, *Gerthsen Physik*, Springer-Verlag, Berlin/Heidelberg, **2006**.

[13] M. Henzler, W. Göpel, *Oberflächenphysik Des Festkörpers*, Vieweg+Teubner, Stuttgart, **1994**.

[14] K. Hermann, *Crystallography and Surface Structure*, Wiley-VCH Verlag GmbH & Co. KGaA, Weinheim, Germany, **2011**.

[15] C. Chang, *Surface Science* **1971**, *25*, 53–79.

[16] G. Wedler, *Lehrbuch Der Physikalischen Chemie*, Wiley-VCH Verlag GmbH & Co. KGaA, Weinheim, Germany, **2004**.

[17] O. Y. Kolesnychenko, Y. A. Kolesnichenko, O. I. Shklyarevskii, H. van Kempen, *Physica B: Condensed Matter* **2000**, *291*, 246–255.

[18] T. König, G. H. Simon, H.-P. Rust, G. Pacchioni, M. Heyde, H.-J. Freund, *Journal of the American Chemical Society* **2009**, *131*, 17544–5.

[19] G. Binnig, K. Frank, H. Fuchs, N. Garcia, B. Reihl, H. Rohrer, F. Salvan, A. Williams, *Physical Review Letters* **1985**, *55*, 991–994.

[20] W. Ho, *The Journal of Chemical Physics* **2002**, *117*, 11033.

[21] Y. Sugimoto, P. Pou, M. Abe, P. Jelinek, R. Pérez, S. Morita, O. Custance, *Nature* **2007**, *446*, 64–7.

[22] P. A. Redhead, E. E. Division, *Vacuum* **1962**, *12*, 203–211.

[23] H. Schlichting, D. Menzel, *Surface Science* **1993**, *285*, 209–218.

[24] H. Schlichting, D. Menzel, *Review of Scientific Instruments* **1993**, *64*, 2013.

[25] J. H. Gross, *Mass Spectrometry: A Textbook*, Springer, **2004**.

[26] R. Wichtendahl, M. Rodriguez-Rodrigo, U. Härtel, H. Kuhlenbeck, H.-J. Freund, *physica status solidi (a)* **1999**, *173*, 93–100.

[27] M. Sterrer, T. Risse, H.-J. Freund, *Applied Catalysis A: General* **2006**, *307*, 58–61.

[28] P. Feulner, D. Menzel, **1980**, *662*, 17–19.

[29] M. Sterrer, T. Risse, H.-J. Freund, *Surface Science* **2005**, *596*, 222–228.

[30] P. Feulner, D. Menzel, *Journal of Vacuum Science and Technology* **1980**, *17*, 662.

[31] H. Schlichting, *Temperature Controller HS 120 / HS 130 Manual*, Schlichting, Gilching, **2000**.

[32] A. M. Ferrari, S. Casassa, C. Pisani, S. Altieri, A. Rota, S. Valeri, *Surface Science* **2005**, *588*, 160–166.

[33] S. Schintke, S. Messerli, M. Pivetta, F. Patthey, L. Libioulle, M. Stengel, A. De Vita, W.-D. Schneider, *Physical Review Letters* **2001**, *87*, 276801.

[34] S. Valeri, S. Altieri, U. del Pennino, a. di Bona, P. Luches, A. Rota, *Physical Review B* **2002**, *65*, 245410.

[35] S. Sicolo, L. Giordano, G. Pacchioni, *The Journal of Physical Chemistry C* **2009**, *113*, 16694–16701.

[36] J. L. Vassent, A. Marty, B. Gilles, C. Chatillon, *Journal of Crystal Growth* **2000**, *219*, 444–450.

[37] D. J. Keavney, E. E. Fullerton, S. D. Bader, *Journal of Applied Physics* **1997**, *81*, 795.

[38] J. L. Vassent, M. Dynna, A. Marty, B. Gilles, G. Patrat, *Journal of Applied Physics* **1996**, *80*, 5727.

[39] W. Wulfhekel, M. Klaua, D. Ullmann, F. Zavaliche, J. Kirschner, R. Urban, T. Monchesky, B. Heinrich, *Applied Physics Letters* **2001**, *78*, 509.

[40] M. Klaua, D. Ullmann, J. Barthel, W. Wulfhekel, J. Kirschner, R. Urban, T. Monchesky, a. Enders, J. Cochran, B. Heinrich, *Physical Review B* **2001**, *64*, 134411.

[41] H. Meyerheim, R. Popescu, N. Jedrecy, M. Vedpathak, M. Sauvage-Simkin, R. Pinchaux, B. Heinrich, J. Kirschner, *Physical Review B* **2002**, *65*, 144433.

[42] H. Meyerheim, R. Popescu, J. Kirschner, N. Jedrecy, M. Sauvage-Simkin, B. Heinrich, R. Pinchaux, *Physical Review Letters* **2001**, *87*, 076102.

[43] M.-C. Wu, J. S. Corneille, C. A. Estrada, J. He, D. Wayne Goodman, *Chemical Physics Letters* **1991**, *182*, 472–478.

[44] S. Benedetti, P. Torelli, S. Valeri, H. Benia, N. Nilius, G. Renaud, *Physical Review B* **2008**, *78*, 195411.

[45] F. Stavale, N. Nilius, H.-J. Freund, *New Journal of Physics* **2012**, *14*, 033006.

[46] M. Sterrer, T. Risse, U. Martinez Pozzoni, L. Giordano, M. Heyde, H.-P. Rust, G. Pacchioni, H.-J. Freund, *Physical Review Letters* **2007**, *98*, 096107.

[47] A. Tekiel, S. Fostner, J. Topple, Y. Miyahara, P. Grütter, *Applied Surface Science* **2013**, *273*, 247–252.

[48] O. Dugerjav, H. Kim, J. M. Seo, *AIP Advances* **2011**, *1*, 032156.

[49] B. Yu, J.-S. Kim, *Physical Review B* **2006**, *73*, 125408.

[50] H. Oh, S. B. Lee, J. Seo, H. G. Min, J.-S. Kim, *Applied Physics Letters* **2003**, *82*, 361.

[51] A. Cattoni, D. Petti, S. Brivio, M. Cantoni, R. Bertacco, F. Ciccacci, *Physical Review B* **2009**, *80*, 104437.

[52] R. G. Musket, W. McLean, C. A. Colmenares, D. M. Makowiecki, W. J. Siekhaus, *Applications of Surface Science* **1982**, *10*, 143–207.

[53] M. Grunze, *Journal of Vacuum Science & Technology A: Vacuum, Surfaces, and Films* **1988**, *6*, 1266.

[54] H. J. Grabke, W. Paulitschke, G. Tauber, H. Viefhaus, *Surface Science* **1977**, *63*, 377–389.

[55] A. J. Pignocco, G. E. Pellissier, *Journal of The Electrochemical Society* **1965**, *112*, 1188.

[56] V. E. Henrich, P. A. Cox, *The Surface Science of Metal Oxides*, Cambridge University Press, Cambridge, **1994**.

[57] E. R. Jette, F. Foote, *The Journal of Chemical Physics* **1933**, *1*, 29.

[58] M. E. Fleet, *Acta Crystallographica Section B Structural Crystallography and Crystal Chemistry* **1981**, *37*, 917–920.

[59] C. Greaves, *Journal of Solid State Chemistry* **1983**, *49*, 325–333.

7. Selbstständigkeitserklärung

Hiermit versichere ich, dass ich die vorliegende Masterarbeit selbständig und lediglich unter Benutzung der angegebenen Quellen und Hilfsmittel verfasst zu haben. Diese Masterarbeit wurde in gleicher oder ähnlicher Form in keinem anderen Studiengang als Prüfungsleistung vorgelegt.

Ort, Datum Unterschrift

8. Attachment

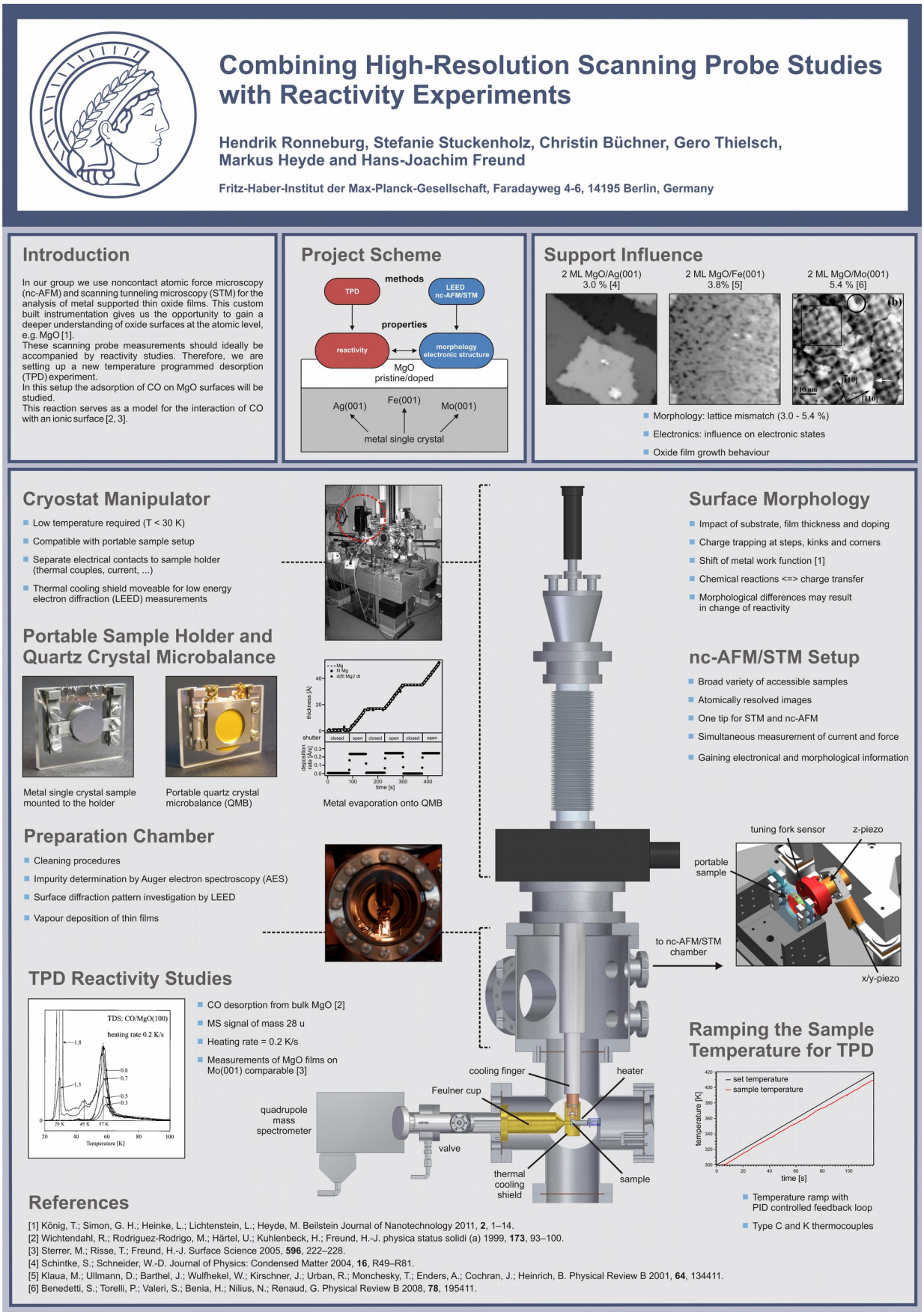

Figure 8.1: Poster presented at the DPG Spring Meeting, Condensed Matter Section, March 2013.

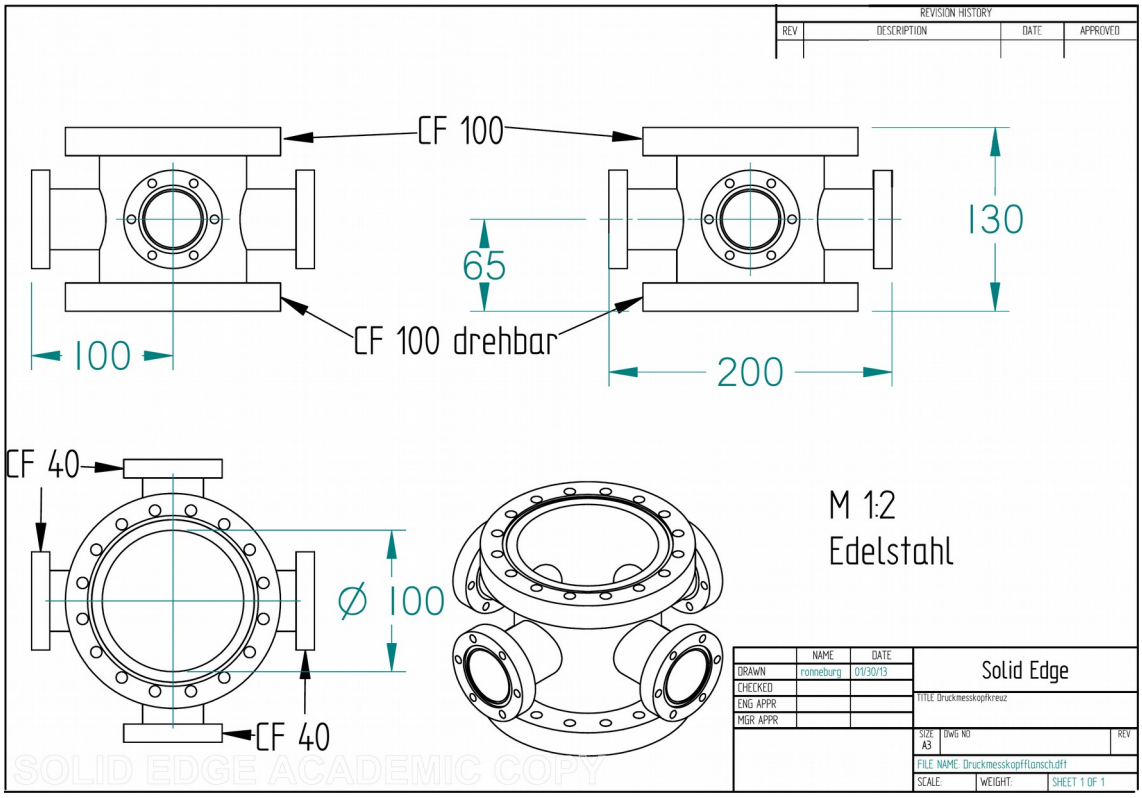

Figure 8.2: Flange cross for pressure gauges, implemented underneath TPD flange cross.

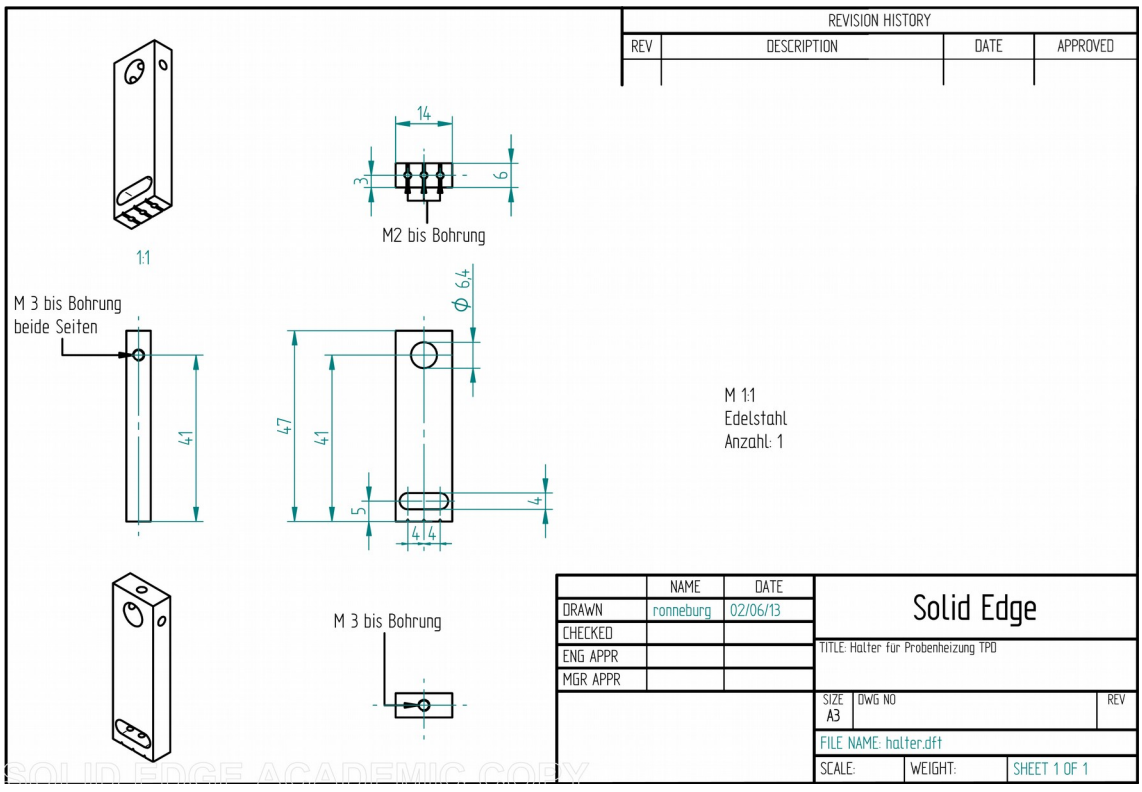

Figure 8.3: Holder, to be mounted onto the transfer rod of the heater.

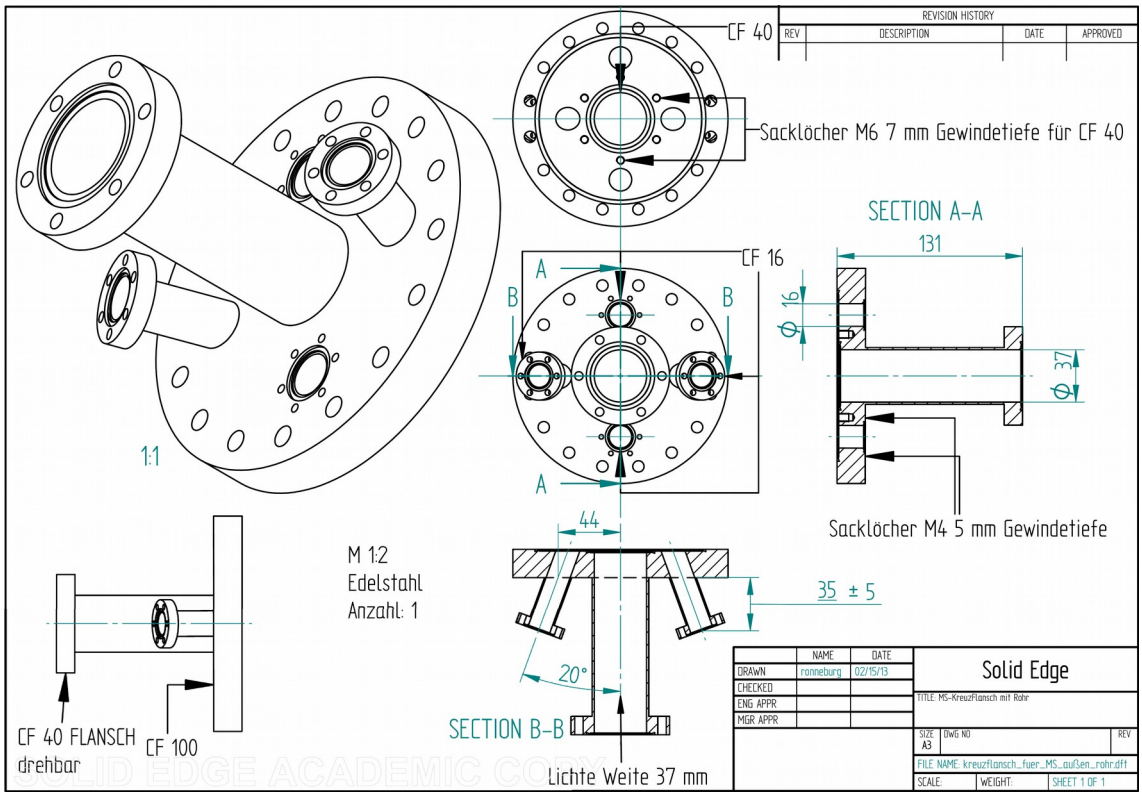

Figure 8.4: Flange, to connect mass spectrometer, valves and TPD flange cross.

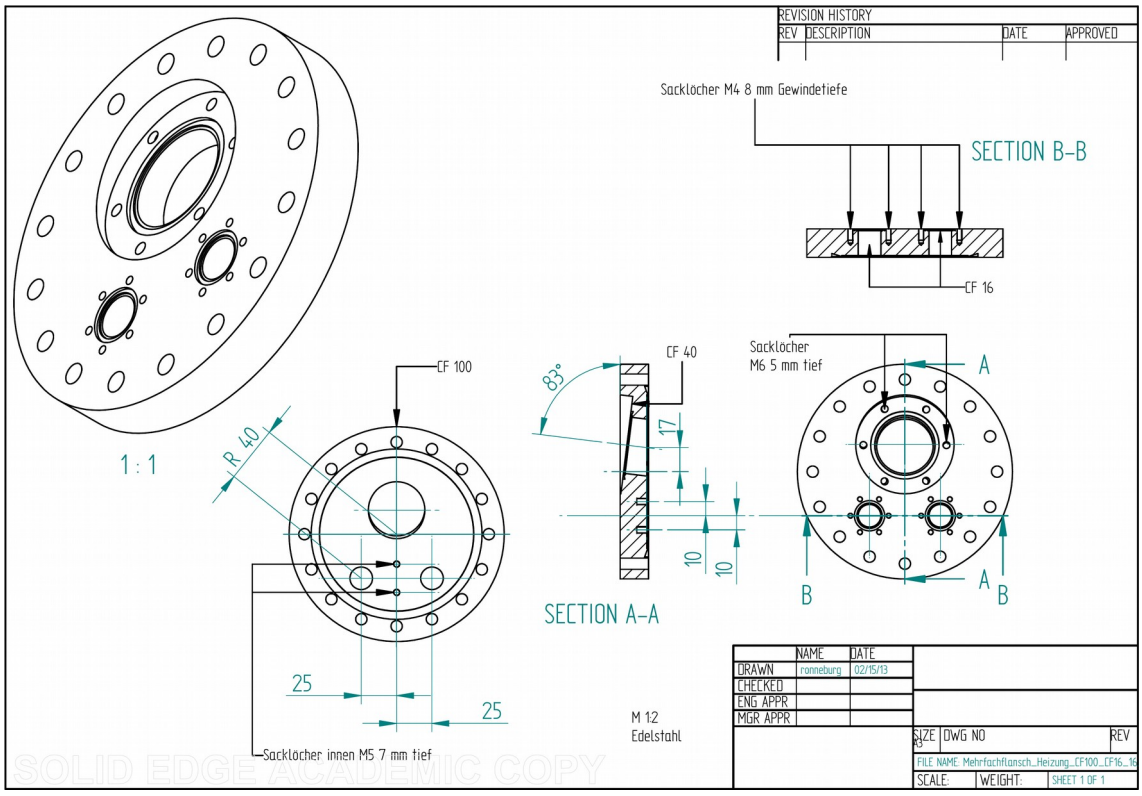

Figure 8.5: Flange, to connect heater, transfer rod and view port with TPD flange cross.

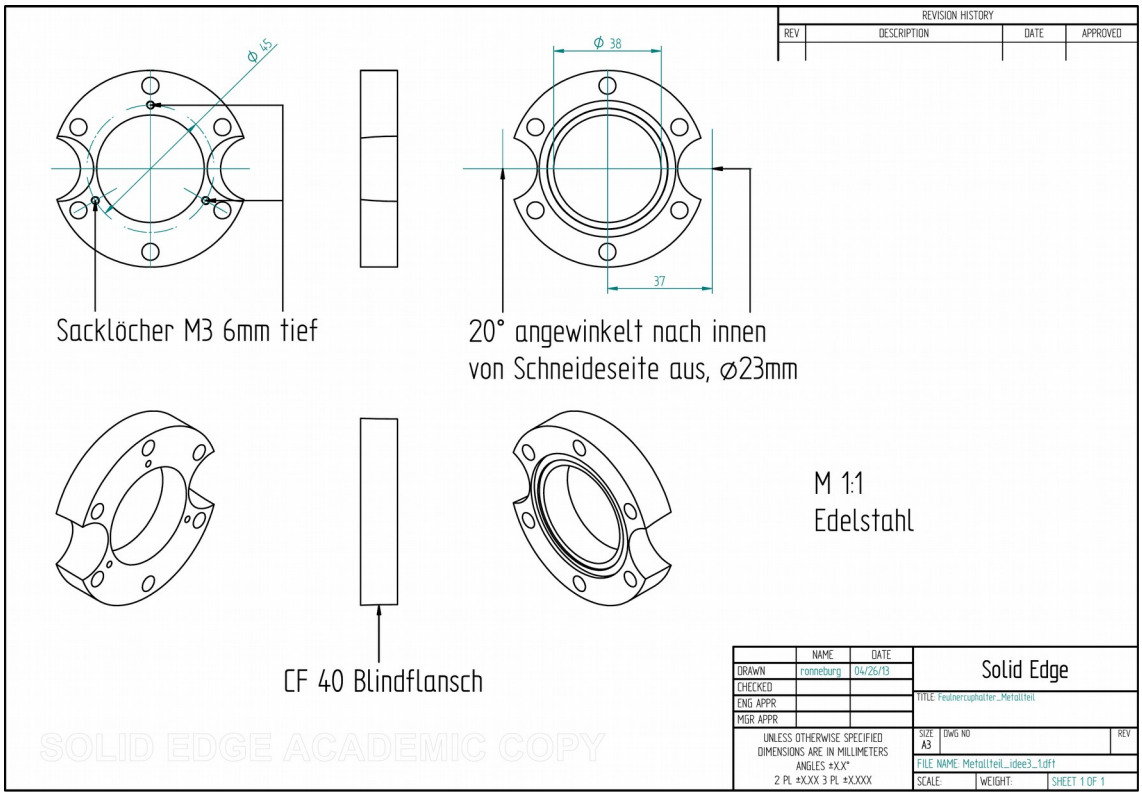

Figure 8.6: Base for Feulner cup

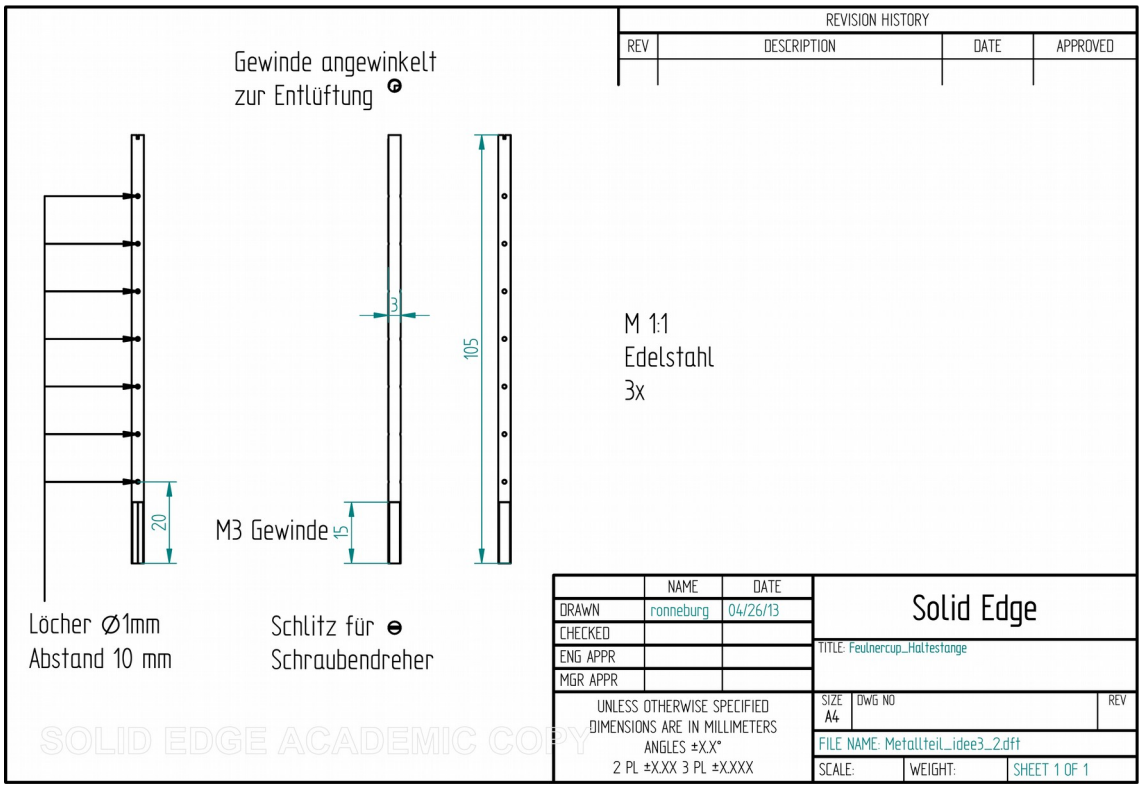

Figure 8.7: Three supporting rods for Feulner cup